UNICA UNIVERSITÀ DEGLI STUDI DI CAGLIARI

Design, Synthesis and Pharmacological Evaluation of Dual FXR-LIFR Modulators for the Treatment of Liver Fibrosis

Pasquale Rapacciuolo,[1,°] Claudia Finamore,[1,°] Cristina Di Giorgio,[2] Bianca Fiorillo,[1] Carmen Massa,[2] Ginevra Urbani,[2] Silvia Marchianò,[2] Martina Bordoni,[2] Chiara Cassiano,[1] Elva Morretta,[1] Lucio Spinelli,[1] Antonio Lupia,[3] Federica Moraca,[1] Michele Biagioli,[2] Valentina Sepe,[1,*] Maria Chiara Monti,[1] Bruno Catalanotti,[1] Stefano Fiorucci,[2] Angela Zampella[1]

[1] Department of Pharmacy, University of Naples "Federico II", Via D. Montesano, 49, I-80131 Naples, Italy

[2] Department of Medicine and Surgery, University of Perugia, Piazza L. Severi, 1, 06132 Perugia, Italy

[3] Department of Life and Environmental Sciences, University of Cagliari, Via Università, 40, 09124 Cagliari, Italy

°Contributed equally to this work.

*To whom correspondence should be addressed.

Valentina Sepe Phone: (+39) 081678526 Fax (+39) 081-678552 E-mail: valentina.sepe@unina.it

Abstract.

Although multiple approaches have been suggested, treating mild-to-severe fibrosis in the context of metabolic dysfunction associated liver disease (MASLD) remains a challenging area in drug discovery. Pathogenesis of liver fibrosis is multifactorial, and pathogenic mechanisms are deeply intertwined; thus, it is well-accepted that future treatment requires the development of multitarget modulators.

Harnessing the 3,4,5-trisubstituted isoxazole scaffold, previously described as key moiety in Farnesoid X Receptor (FXR) agonism, herein we report the discovery of a novel class of hybrid molecules endowed with dual activity towards FXR and the Leukaemia Inhibitory Factor Receptor (LIFR). Up to 27 new derivatives were designed and synthesized. The pharmacological characterization of this series resulted in the identification of **3a** as a potent FXR agonist and LIFR antagonist with excellent ADME properties. *In vitro* and *in vivo* characterization identified compound **3a** as the first-in-class hybrid LIFR inhibitor and FXR agonist that protects against the development of acute liver fibrosis and inflammation.

Introduction

Fibrosis, that typically develops in the context of chronic liver damage due to infectious (HBV and HCV), toxic/drug-induced (mainly alcohol-induced), metabolic (such as metabolic dysfunction-associated fatty liver disease-MAFLD), cholestatic, or autoimmune insults, is the major determinant of the clinical outcome in patients suffering from chronic liver diseases. [1,2] Cirrhosis is defined as an advanced stage of fibrosis, associated with the formation of regenerative nodules of liver parenchyma that are separated by fibrotic septa and encapsulated in it.[3] Hepatic fibrosis, once regarded as a passive and irreversible process, is now considered as a dynamic setting, where active fibrogenesis, which leads to accumulation of extracellular matrix (ECM), coexists with matrix degradation and tissue remodeling.[4] In this novel conceptual landscape, liver fibrosis has emerged as a potential therapeutic target in the treatment of chronic liver disorders.[5]

The key effectors of the fibrogenic response, at least in non-bile duct related disorders, are hepatic stellate cells (HSCs).[6] HSCs reside in a quiescent state in the homeostatic liver, but they are activated by a continuous liver damage. [7] Activated HSCs might transdifferentiate into myofibroblasts, becoming the major responsible for fibrillar ECM deposition, but also for the release of pro-inflammatory cytokines, chemokines, and other mediators, such as transforming growth factor-β (TGF-β), platelet-derived growth factor (PDGF), and vascular endothelial growth factor (VEGF) that perpetuate ECM deposition and inflammation.[1,7,8]

While in the last decade several potentially druggable molecular mechanisms have been identified, [9] targeting fibrosis has proven difficult and many drug candidates have failed in clinical trials.[10,11] Nevertheless, several orally active molecules are currently advanced for treating mild-to-severe fibrosis in the context of metabolic dysfunction associated liver disease (MASLD), [12] a challenging area in drug discovery.[11] These novel approaches include elafibranor, a pan-Peroxisome Proliferator-Activated Receptors (PPAR) activator,[13] various steroidal and non-steroidal ligands of the Farnesoid

X Receptor (FXR) such as obeticholic acid[4,15] and cilofexor,[16] the latter belonging to the well-known "isoxazole-family", cinecriviroc, a C-C chemokine receptor (CCR) 2/5 antagonist, [10] resmetirom, a thyroid hormone receptor β antagonist, [17] single Glucagon Like peptide-1 (GLP-1) receptor agonists like semaglutide[1] and dual GLP1-RA/glucose induced polypeptide (GIP) agonists such as tirzepatide,[18] Lysyl Oxidase Like 2 (LOXL2) inhibitors, Pan-caspase inhibitors, or TGF-β signaling inhibitors.[19] Unfortunately, most of these agents have failed to achieve the prespecified endpoints in clinical trials,[11] and only resmetirom has gained approval for treating stage 2 and 3 (F2 and F3) liver fibrosis in MASH patients in March 2024, although 70-80 % of participants to the MAESTRO-NASH trial did not respond to treatment according to histological criteria.[17]

Even though several reasons might explain the high rate of drug failure in phase 3 clinical trials in MASLD patients,[20] one mechanistic hypothesis is that the pathogenesis of liver fibrosis is multifactorial and pathogenic mechanisms are deeply intertwined, requiring the development of multitarget modulators.[21,22]

Bile acids-regulated receptors (BARRs) are a group of nuclear and cell membrane receptors activated by primary and secondary bile acids.[23] FXR[24] and the membrane G protein-coupled bile acid receptor 1 (GPBAR1),[25] two widely expressed BARRs, regulate multiple signaling pathways and play important roles in hepatic lipid metabolism, inflammation, immune responses and fibrosis. [22,23,26,27]

Some FXR agonists have completed phase 2 and 3 trials in MASLD patients, and while the approval for clinical use of obeticholic acid in MASLD was denied by the Food and Drug Administration (FDA) in 2023 because the severity of side effects, cilofexor is still under development.[28] Nevertheless, results from the REGENERATE study[14] have confirmed that FXR agonism effectively reverses liver fibrosis, confirming early evidence that FXR agonism could exert anti-fibrotic effects[29] and suggesting that FXR agonism still holds potential in MASLD area to avoid potential side effects linked to the use of obeticholic acid.[30]

The leukaemia inhibitory factor receptor (LIFR) and its endogenous ligand, the leukaemia inhibitory factor (LIF), have attracted increasing attention for their role in inflammation, fibrosis and oncogenesis.[31] LIF is a member of the interleukin-6 (IL-6) cytokines family, displaying an important role in many physiological and pathological processes.[32,33]

LIFR is constituted by two transmembrane proteins, LIFRβ and glycoprotein-130 (gp130).[34,35] LIFRβ can heterodimerize with gp130 and/or other transmembrane proteins such as Oncostatin M.[36] LIFRβ–gp130 complex is the actual mediator of the signal transduction upon LIF binding.[36] Upon binding, LIFR activation promotes the JAK-STAT3 pathway, thereby modulating the expression of several transcription factors regulating initiation, progression and metastasis in cancer.[33] A dysregulation of IL-6 signaling contributes to inflammation-associated conditions, such as obesity, some inflammatory-bowel diseases (IBDs), inflammatory arthritis and fibrosis, including renal interstitial fibrosis.[37–39]

To date, no anti-LIFR agents have been approved for clinical use, although a specific anti-LIFR antibody and orally active small molecules have been identified to antagonize the LIF-LIFR axis, including EC359, mifepristone, LRI201 and some natural and semisynthetic bile acids.[31,40–42] Recently, we have reported that endogenous bile acids and semisynthetic alcohol derivatives of endogenous bile acids[43] function as LIF-LIFR antagonists reverting proliferation and LIF-dependent oncogenesis in a model of pancreatic ductal adenocarcinoma (PDAC)[43] and gastric adenocarcinoma (GC).[42]

These findings, and in particular the discovery that well-known steroidal FXR agonists, such as bile acids and their alcoholic derivatives, were able in antagonizing LIFR, suggested us that other chemical scaffolds of FXR agonists could also be able of inhibiting LIFR. Moreover, from a pharmacological point of view, we also considered that the possible synergy among FXR agonism, counteracting metabolic dysfunctions and LIFR antagonism turning off IL-6 inflammation signaling,

both associated with fibrosis development and progression, might be the basis of a novel multi-target strategy against liver fibrosis. These consideration prompt us to further investigate FXR agonists as possible dual inhibitors endowed with LIFR antagonism activity.

To pursue this aim, we focused our attention on a class of potent non-steroidal FXR agonists characterized by the isoxazole core, previously developed.[44,45]

Accordingly, we selected GW4064 (EC_{50} = 0.058 μM),[50] the prototype of isoxazole-type FXR agonists, and compounds **1a**, **1b,** and **1c** (Figure 1A and Scheme 1), previously synthesized in our laboratories,[49] and screened their *in vitro* activity on LIF-LIFR macromolecular complex. Confirming our insight, these compounds showed good efficacies and good potencies towards LIFR (Figure 1A).

Thus, in this paper we will discuss the exploration of the chemical space around the isoxazole core due to its structural flexibility, with the aim to develop compounds endowed with dual FXR agonistic and LIFR antagonistic activity, endowed with improved ADME profiles and reduced toxicity with respect to GW4064,[46] and readily accessible through organic synthesis.

Synthesis, along with pharmacological and computational investigations, led to the identification of compound **3a** as both FXR agonist and LIFR antagonist. Collectively, in this study, we introduce the first synthetic dual modulator of FXR and LIFR as potential agent for the treatment of liver fibrosis.

Results

Keeping the same substitutions at C3 and C5 of **1a**, **1b**, and **1c**,[44] we explored first the substitution at C4, obtaining compounds **1d**, **1e**, **1f**, **1g,** and **1h** (Figure 1B and Scheme 1) by changing either the reciprocal positions of the C4-two phenyl rings or the position of the carboxylate end-group.

Then, starting from compounds **1b**, **1c**, and **1h,** representing the best parents in terms of efficacy, potency, and PK profile, the exploitation of the chemical space first at positions C3 and then at position C5 of the isoxazole core afforded compounds **2a-2h** (Figure 1C and Scheme 2) and **3a-3e** (Figure 1D and Scheme 3), respectively.

Considering the good activity towards both FXR and LIFR of compound **3e** (see below, Figure 2), the *t*-butyl group at C5 was fixed while positions C3 and C4 were further modified, obtaining compounds **4a-4i** (Figure 1E and Scheme 4).

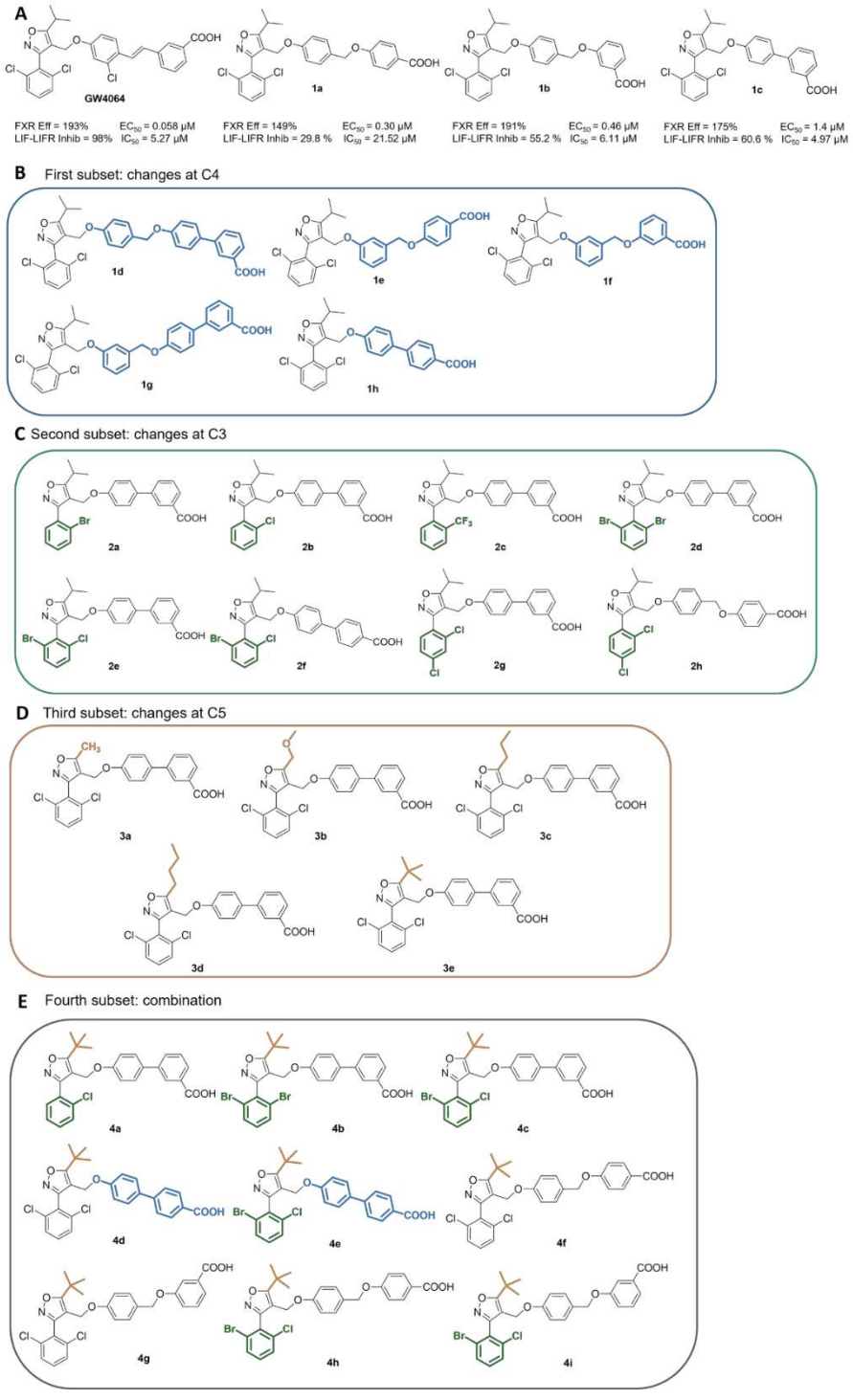

Figure 1. (A) Isoxazole previously reported. [44] (B) Isoxazole modified at C4. (C) New isoxazoles modified at C3. (D) Modificaton at C5. (E) Chemical structure of new isoxazoles with t-Bu at C5 and modified at C3 and/or at C4

Chemical synthesis. The synthesis of compounds **1a**, **1b**, and **1c** was performed as previously described.[44] Compounds **1d-1h** were prepared as illustrated in Scheme 1. The commercially available 2,6-dichlorobenzaldehyde was cyclized to form 3,4,5-trisubstituted isoxazole and, using the Mitsunobu reaction, several hydroxybenzoates, differently substituted on the phenyl ring, were coupled to the isoxazolyl alcohol obtaining compounds **6** and **7**. As Mitsunobu coupling led to scarce yields when methyl 4'-hydroxybiphenyl-4-carboxylate was used, we performed mesylation of the alcohol followed by Williamson ether synthesis, obtaining the methyl ester **14**, in turn hydrolyzed to give **1h.** The reduction of compound **6** methyl ester group with $LiBH_4$ gave alcohol **8**, which, in turn, was coupled *via* Williamson reaction to give the methyl ester **10**. Its alkaline hydrolysis afforded carboxylic acid **1d** (Scheme 1). The same protocols were applied to obtain compounds **1e-1g** from alcohol **9**.

Scheme 1. Synthesis of Compounds 1a−h[a]

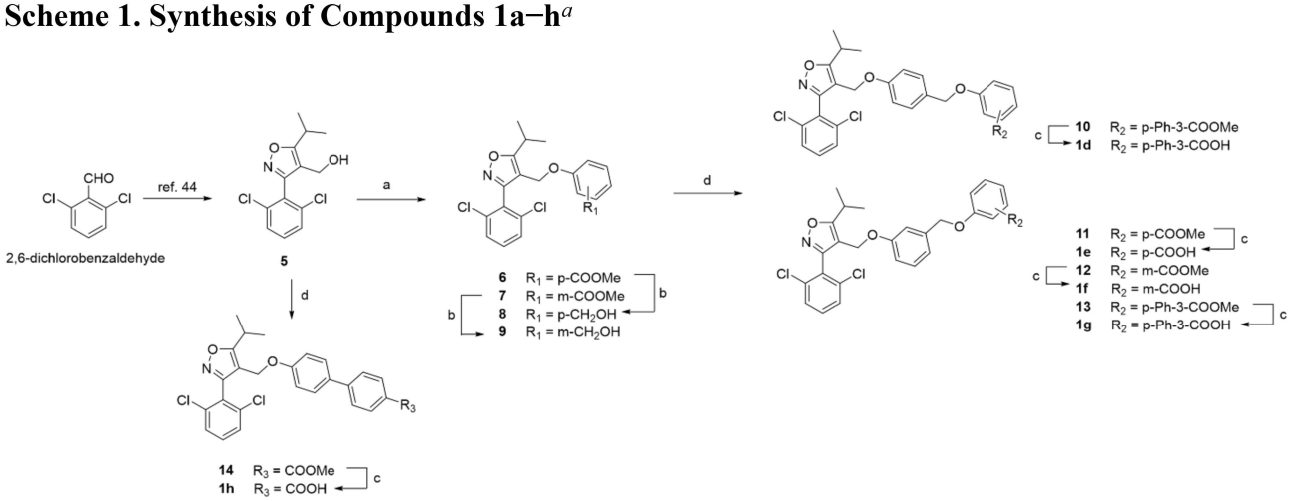

[a]*Reagents and Conditions*. a) Different hydroxybenzoates, PPh_3, DIAD in THF dry, 0°C, 23%-65%; b) $LiBH_4$, MeOH dry, in THF dry, 0°C, 80%-95%; c) NaOH, in MeOH/H_2O 1:1 v/v, reflux, 44%-95%; d) 1. Methanesulphonyl chloride, triethylamine, dry THF, -20°C; 2. Methyl 4'-hydroxybiphenyl-4-carboxylate, K_2CO_3, dry DMF, 100°C, 49%-78% over 2 steps.

The versatility of this synthetic strategy allowed us to introduce different substitutions on the isoxazole core. Changing alternately the starting materials, different aldehydes or different β-ketoesters, as described in the Experimental Section, we obtained two different subsets depending on C3 or C5 isoxazole modifications.

Following the same procedure previously described in Scheme 1, compounds **2a-f** and compounds **3a-3e** were synthesized in good yields (Scheme 2 and 3, respectively).

Scheme 2. Synthesis of Compounds 2a−h[a]

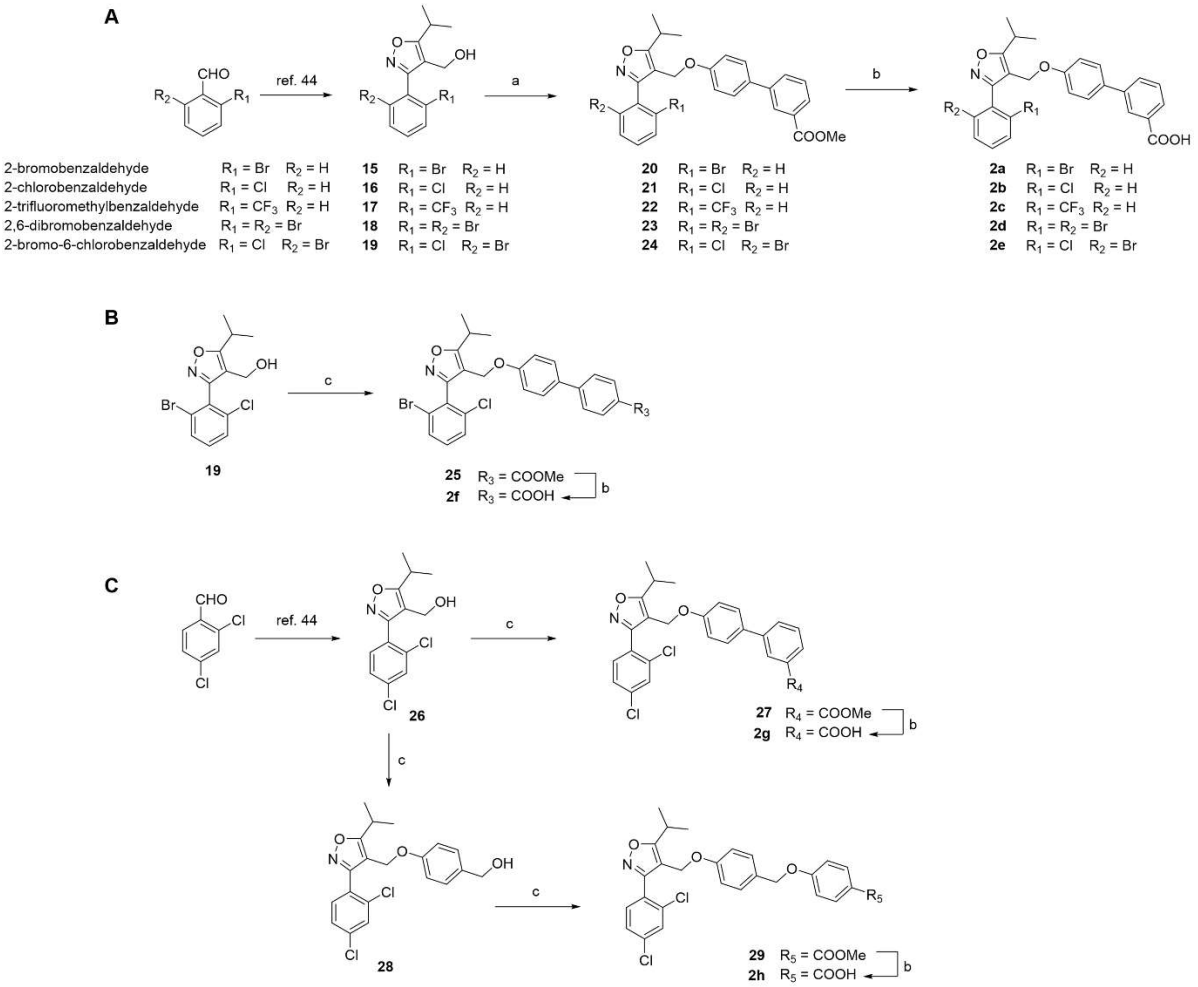

[a]*Reagents and Conditions*. a) PPh_3, DIAD, methyl 4-hydroxybenzoate or methyl 4'-hydroxybiphenyl-3-carboxylate, THF dry, 0° C, 15%-87%; b) NaOH, MeOH/H_2O 1:1 v/v, 34%-96%; c) 1. Methanesulphonyl chloride, triethylamine, dry THF, -20°C; 2. Methyl 4'-hydroxybiphenyl-4-carboxylate, K_2CO_3, dry DMF, 100°C, 80%-84% over 2 steps; d) $LiBH_4$, MeOH dry, in THF dry, 0°C, 86%.

Scheme 3. Synthesis of Compounds 3a−e[a]

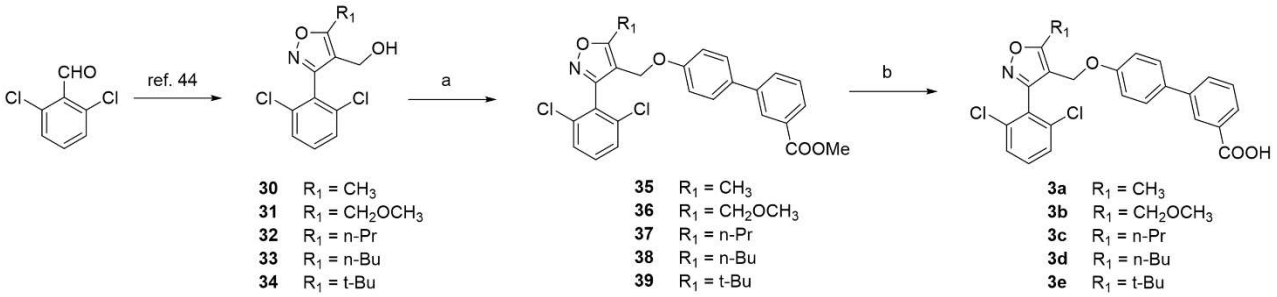

[a]*Reagents and Conditions*. a) PPh_3, DIAD, methyl 4'-hydroxybiphenyl-3-carboxylate, THF dry, 0° C, 46%-98%; b) NaOH, MeOH/H_2O 1:1 v/v, 48%-99%.

Finally, by retaining the *t*-butyl group at C5 and switching either the benzaldehydes or the substitution at C4, compounds **4a-4i** (Scheme 4) were obtained.

Scheme 4. Synthesis of Compounds 4a−i[a]

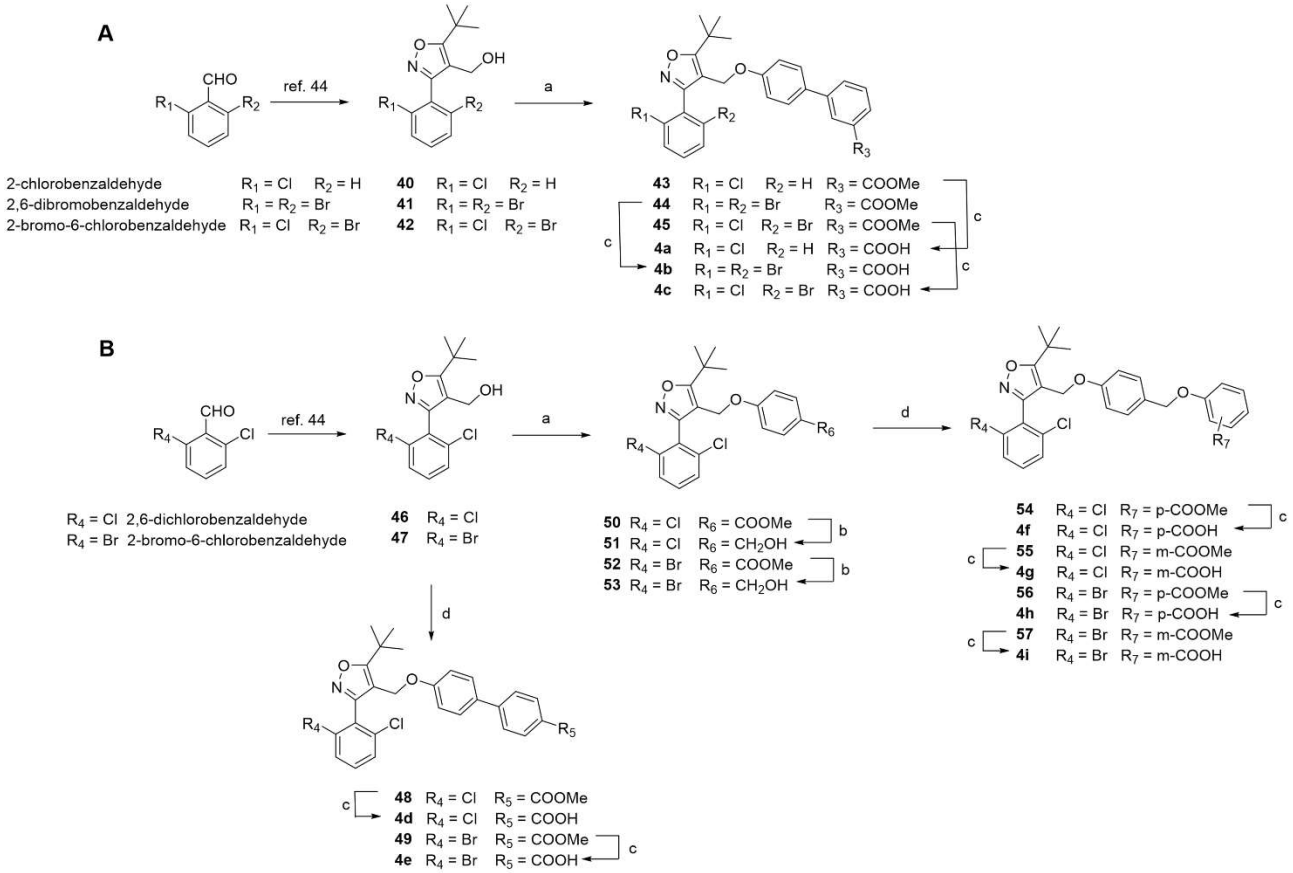

[a]*Reagents and Conditions*. a) Different phenols, PPh_3, DIAD in THF dry, 0°C, 12%-79%; b) $LiBH_4$, MeOH dry, in THF dry, 0°C, 79%-94%; c) NaOH, in MeOH/H_2O 1:1 v/v, reflux, 48%-98%; d) 1. Methanesulphonyl chloride, triethylamine, dry THF, -20°C; 2. Methyl 4'-hydroxybiphenyl-4-carboxylate, K_2CO_3, dry DMF, 100°C, 41%-59%.

In vitro assays

All twenty-seven new isoxazole derivatives were tested at 5 μM in a cell-free AlphaScreen Assay for FXR agonism. Chenodeoxycholic acid (CDCA) was used as control at 20 μM and its effect was settled at 100%. Likewise, LIF-LIFR inhibitory activity was analysed using AlphaScreen testing the twenty-seven new molecules together with **1a**, **1b**, and **1c**, at 10 μM. The signal registered by LIF-LIFR interaction without any compound was taken as 100% of interaction. The results of the *in vitro* efficacies and potencies were summarized in Figure 2.

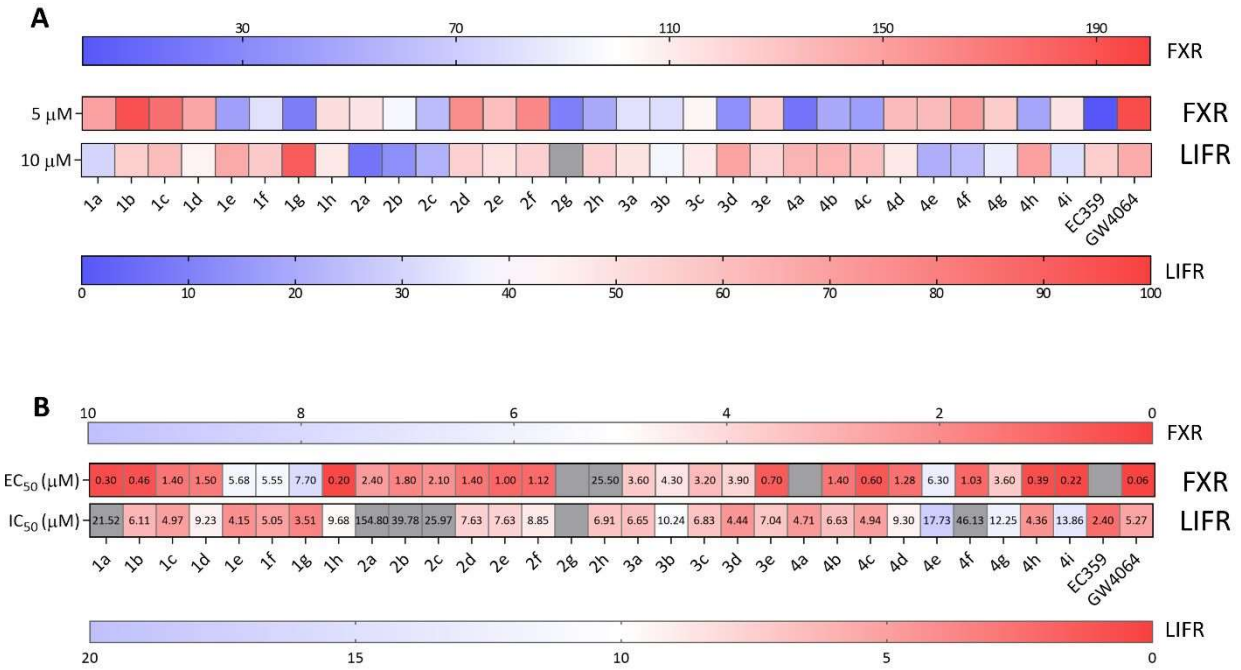

Figure 2. Heat maps of *in vitro* activity of isoxazole derivatives. Panel **A**: each box represents the efficacy of a single compound towards FXR (upper row) and LIF-LIFR (lower row) assessed by cell-free AlphaScreen Assays. Compounds were tested at 5 μM for FXR and 10 μM for LIF-LIFR. Panel **B**: each box indicates the EC_{50} (upper row) and IC_{50} (lower row) for FXR and LIF-LIFR, respectively. Full gray boxes indicate values out of range. Empty gray boxes are assumed as not determined.

The following parameters were established to narrow down the consistent number of analyzed compounds: we selected the compounds showing efficacies > 45% for both FXR agonism and LIF-LIFR inhibition with potencies in the range of FXR $EC_{50} < 5$ μM and LIF-LIFR $IC_{50} < 10$ μM. The resulting derivatives (**1h**, **2d**, **2e**, **2f**, **3a**, **3c**, **3e**, **4b**, and **4d**) were judged excellent FXR agonists with EC_{50} ranging from 3.6 to 0.2 μM. At the same time, all of them resulted endowed with a powerful LIF-LIFR inhibitory activity with potencies down to 5 μM (see Figure S1 and S2). The preliminary evaluation of the *in vitro* pharmacokinetic (PK) properties of the ten candidates was characterized by LC-MS analysis and reported in Figure 3.

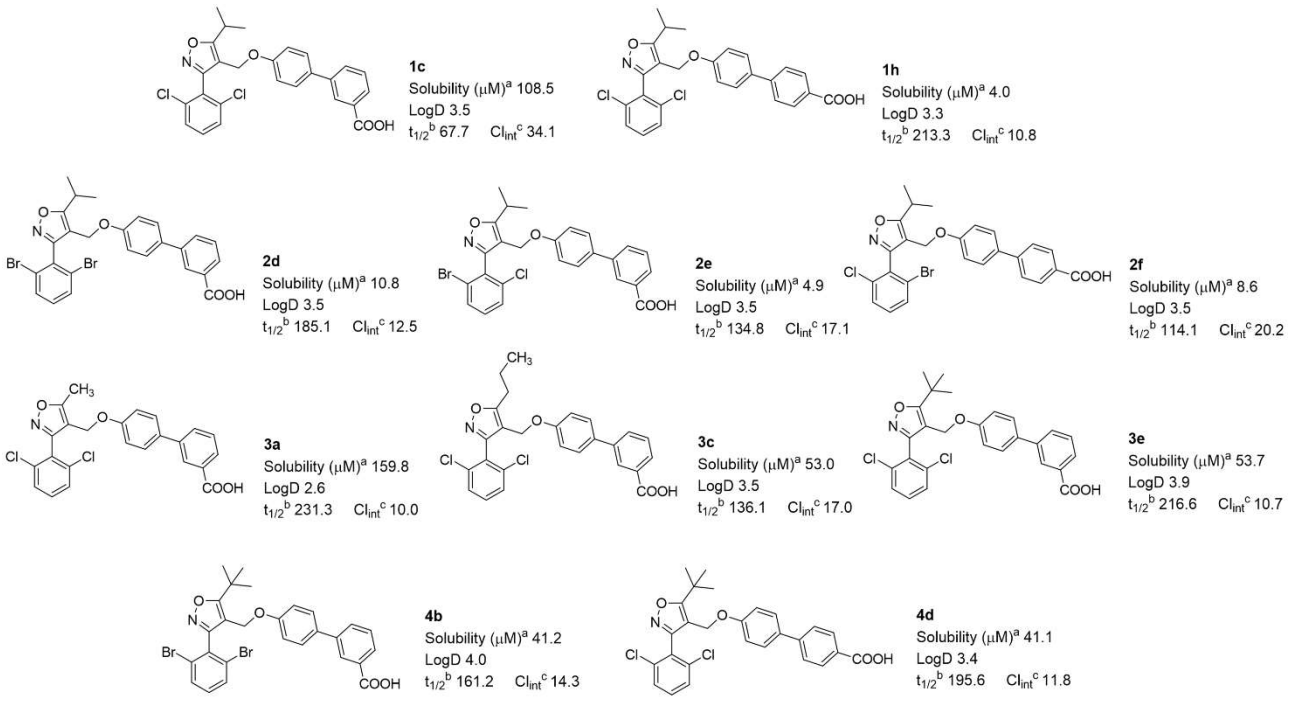

Figure 3. ***In vitro*** **pharmacokinetics parameters.** [a]Aqueous solubility at pH 7.4; [b]Reported in minutes; [c]Reported as μL/min/mg protein. Results are mean of at least two experiments.

All compounds showed improved metabolic stabilities with respect of the parent compound **1c** in liver S9 fraction, with half-life ($t_{1/2}$) values greater than 100 min. They also showed good logDs and excellent solubility, higher than 40 μM, except for compounds **1h**, **2d**, **2e**, and **2f**.

Consequently, ruling out the least soluble derivatives, a parallel artificial membrane permeability assay (PAMPA) was performed on compounds **1c**, **3a**, **3c**, **3e**, **4b**, and **4d** (Table 1) to further characterize their PK profile by comparison with GW4064 as reference. In PAMPA, $\log P_{eff}$ values lower than –5.50 are generally associated with very poor cell permeability. Interestingly, all compounds presented $\log P_{eff}$ values higher than –5.40 as shown in Table 1, especially **1c**, **3e**, **3c**, and **4d**, suggesting a very good cell permeability, except for GW4064 which is practically impermeable. These data can be easily noticed considering the %T value, standing for the percentage amount of compound permeated after 5 hours. Compounds **1c**, **3c**, and **4d** presented the highest permeability over time (up to 27.4%) while only 1% of GW4064, the parent compound, was able to pass over 5 hours.

Table 1. PAMPA assay*

	P_{app}	$logP_{app}$	$logP_{eff}$	%T (5h)
GW4064	4.23E-07	-6.37	-6.72	1.21
1c	1.22E-05	-4.91	-5.11	27.32
3a	5.58E-06	-5.25	-5.32	14.29
3c	1.23E-05	-4.91	-5.12	27.4
3e	4.34E-06	-5.36	-5.71	11.41
4b	4.35E-06	-5.36	-5.34	11.43
4d	6.55E-06	-5.18	-5.45	16.43

*Verapamil was used as control compound for consistency of PAMPA assay

In vitro transactivation on HepG2 and Stellate/Macrophages

The biological activity of these compounds was also assessed in transactivation assays on HepG2 cells, and the results are shown in Table 2 and in Figures S3 and S4. Except for compound **4b**, all compounds showed a significant efficacy toward FXR with potencies in the same micromolar concentration range. Despite the overall excellent behavior on FXR, only compounds **1c**, **3a**, and **4d** showed an inhibitory activity towards LIFR. Given the interest in designing dual modulators, the best two candidates are compounds **3a** (EC_{50} = 3.2 μM and IC_{50} = 2 μM) and **4d** (EC_{50} = 0.34 μM and IC_{50} = 2.5 μM).

Table 2. Efficacy and potency towards FXR and LIFR on HepG2

Compound	FXR Eff%	EC_{50} μM	LIF-LIFR Eff%	IC_{50} μM
1c	813.5 ± 24	2.30 ± 0.42	66.1 ± 0.6	8.2 ± 0.2
3a	350 ± 12	3.20 ± 0.28	57.8 ± 4.7	2.0 ± 1.9
3c	371.3 ± 29	2.00 ± 0.25	33 ± 6.4	49.0 ± 7.5
3e	812.2 ± 24	3.20 ± 0.98	66 ± 5	34.4 ± 1.2
4b	146 ± 7.8	2.10 ± 0.07	59.2 ± 8.5	6.7 ± 2.0
4d	458 ± 74	0.34 ± 0.02	45.9 ± 7	2.5 ± 1.4

Eff (%) is the maximum efficacy of the compound (10 μM) relative to CDCA (10 μM) as 100% in FXR transactivation and the maximum efficacy of the compound (50 μM) relative to LIF as 100% in LIFR transactivation; EC_{50} and IC_{50} values (μM) were calculated from at least three experiments. Results are expressed as mean ± SD.

Successively, we investigated whether compounds **3a** and **4d** were effective on primary mouse hepatocytes (HepG2). In liver parenchymal cells, FXR activation leads to the regulation of a cohort of genes that function to decrease the synthesis of bile acids and to promote their excretion, preventing the accumulation of potentially harmful bile acids in hepatocytes. The expression of known FXR target genes was measured in presence of either **3a**, **4d**, GW4064, as control for FXR agonism, and EC359, as control for LIF-LIFR antagonism. Compound **3a** confirmed its strong activity towards FXR and significantly up-regulated the relative mRNA expression of canonical FXR target genes such as Shp, a unique member of the nuclear receptor (NR) superfamily, involved in the inhibition of hepatic bile acid synthesis from cholesterol, and Ostα, and Ostβ, (Figure 4, panel A, C and D respectively), the solute carrier proteins, involved in the lateral transport of bile acids. Compound **3a** also inhibited the expression of Cyp7a1, the rate-limiting enzyme involved in the classic pathway of bile acid biosynthesis (Figure 4, panel B). Together, these effects results in suppression of bile acid synthesis by SHP/CYP7A1 mediated pathway while basolateral excretion is increased. [47] The anti-inflammatory activity mediated by LIF was assessed by testing **3a** and **4d** on Raw264.7 macrophages (Figure 5). Compound **3a** exerted a strong inhibitory activity towards LIFR counteracting the production of CCL2,[10] also known as monocytic chemotactic protein 1 (MCP-1), a potent pro-fibrogenic mediator, and IL-6, a pro-inflammatory cytokine. Similar effects were observed with GW4064 and EC359. A similar outcome was observed with compound **4d** which proved to be slightly more efficient in decreasing IL-6 levels than **3a**.

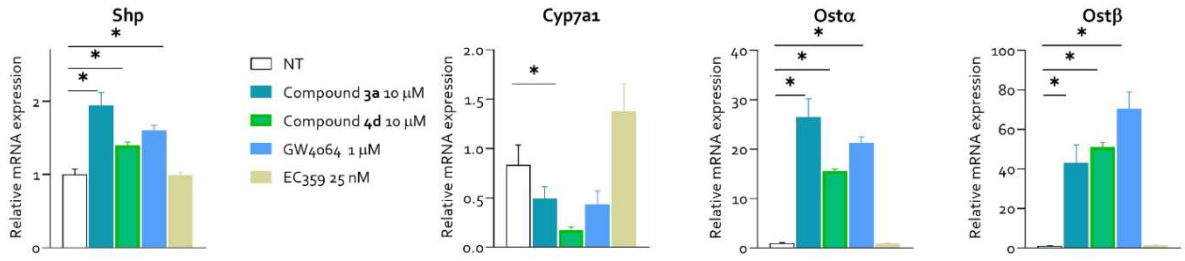

Figure 4. Compounds 3a and 4d act as strong FXR agonists on HepG2 cells. HepG2 cells were exposed to compound **3a** (10 μM), compound **4d** (10 μM), FXR agonist GW4064 (1 μM) and LIFR antagonist EC359 (25 nM) for 24 h or left untreated. The relative mRNA expression of the FXR downstream targets (A) Shp, (B) Cyp7a1, (C) Ostα, and (D) Ostβ

were measured. Each value was normalized to GAPDH. Results are the mean ± SEM of 3 samples for group. (*represents statistical significance: $p < 0.05$).

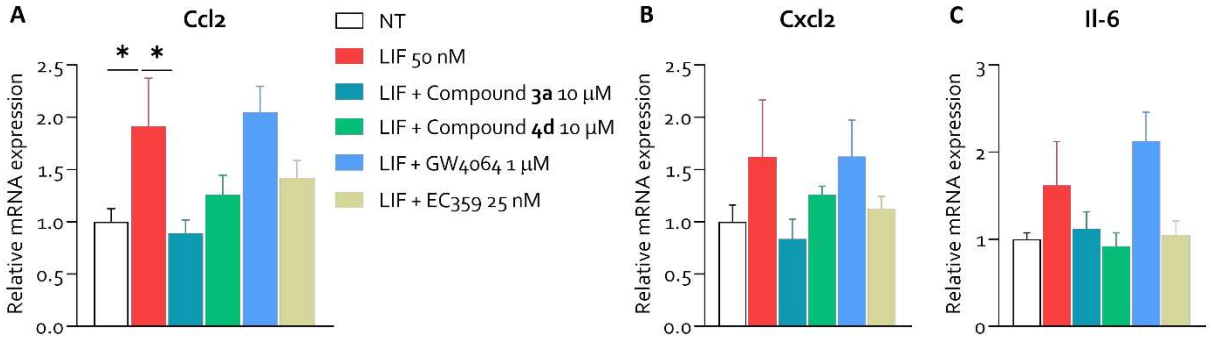

Figure 5. Compounds 3a and 4d counteract the effect of LIF on a murine macrophages cell line. The Raw264.7 cell line was exposed to 50 nM of LIF alone or in combination with compound **3a** (10 µM), compound **4d** (10 µM), FXR agonist GW4064 (1 µM) and LIFR antagonist EC359 (25 nM) for 24 h or left untreated. Relative mRNA expression of the pro-inflammatory mediators (A) Ccl2, (B) Cxcl2 and (C) Il-6 were accessed. Each value was normalized to GAPDH. Results are the mean ± SEM of 3 samples for group. (*represents statistical significance: $p < 0.05$). Where not indicated, the data are not significant.

Consequently, compounds **3a** and **4d** were tested on hepatic stellate cells (HSC) treated with LIF. Compound **4d** showed a comparable activity to that of EC359 in terms of reduction of collagen and α-SMA production, two biomarkers of hepatic stellate cells activation (α-SMA) and ECM deposition (COL1A1). On the other end, compound **3a** presented a better activity over HSC cells as it greatly reduced the amounts of collagen and α-SMA levels (Figure 6).

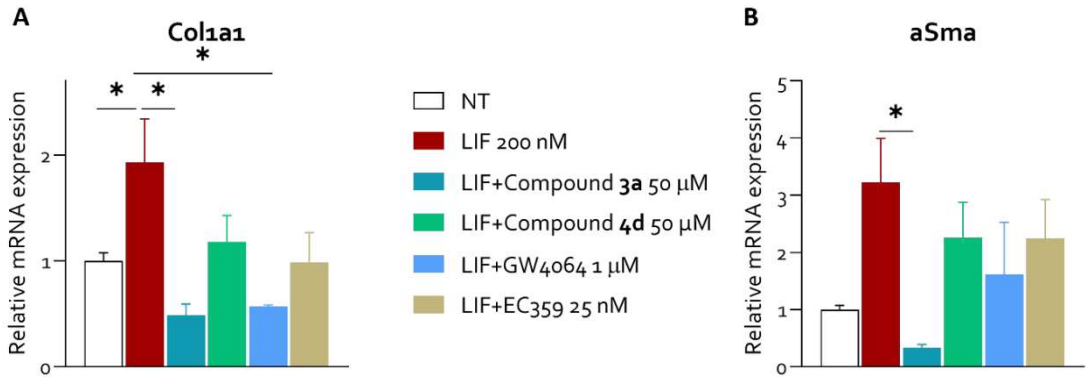

Figure 6. Compound 3a exerted an antifibrotic activity on hepatic stellate cell line. HSC cells were exposed to 200 nM of LIF alone or in combination with compound **3a** (50 µM), compound **4d** (50 µM), FXR agonist GW4064 (1 µM) and LIFR antagonist EC359 (25 nM) for 24 h or left untreated. Relative mRNA expression of the pro-fibrotic (A) Col1a1, and (B) aSma. Each value was normalized to GAPDH. Results are the mean ± SEM of 3 samples for group. (*represents statistical significance: $p < 0.05$).

The overall promising biological activity of **3a**, the leading compound of this library on the tested cell lines, prompted the study of its behavior in a model of fibrosis *in vivo*. To this end, a murine

model of carbon tetrachloride (CCl_4)-induced fibrosis was employed to further explore the potentiality of compound **3a**.

In vivo assay. We have then investigated whether *in vivo* treatment with **3a** effectively reverses hepatic stellate cells activation induced by treating mice with CCl_4, a model for liver fibrogenesis. [1] To this end, mice were administered CCl_4 with or without compound **3a**, at the dose of 3, 10 or 30 mg/kg/day for 1 week (Figure 7A). The results of these studies demonstrated that while treating mice with CCl_4 caused a significant weight drop, systemic inflammation (Figure 7B and 7C) and hepatocytes damage as demonstrated by the increase of AST and ALT, and bilirubin plasma levels (Figure 7D-F), this pattern was reversed by compound **3a**, in a dose-dependent manner, with the doses of 10 mg/kg and 30 mg/kg being the most effective. In contrast, compound **3a** exerted no effects on LDL plasma levels (Figure 7G), that should be viewed as a substantial improvement since selective FXR agonism worsens LDL levels in clinical trials.[48] Additionally, treating mice with CCl_4 promoted HSC activation and collagen deposition as measured by image J analysis of Sirius red-stained livers (Figure 7H). Liver fibrosis induced by a 7-days course of CCl_4 was mild, but significantly attenuated by co-treating animals with **3a** (Figure 7I). Additionally, compound **3a** reversed the expression of various biomarkers of hepatic stellate cells activation (α-SMA and CCL2) and ECM deposition (COL1A1) (Figure 7J-L). Each dose of compound **3a** tested in the study was effective and there was no difference in the effects over the range of 3-30 mg/kg tested. Furthermore, while the liver expression of Lif was increased by treating mice with CCl_4, the pattern was reversed by compound **3a** (Figure 7M). The same regulation, thought to be opposite, [31] was observed for Lifr (Figure 7N). Finally, confirming that compound **3a** behaves as an FXR agonist *in vivo*, we found that treating mice with this agent increased the liver levels of Shp and Ostβ (two FXR target genes, Figure 7P and 7R). In contrast, compound **3a** partially restored the expression of Bsep while increased the expression of Cyp7a1 (Figure 7Q and 7S). The last effect is puzzling, since FXR agonism represses the expression of Cyp7a1, the rate limiting enzyme in the classical pathway of bile acid synthesis in hepatocytes,

suggesting a potential role for LIF in regulating this gene in conjunction with FXR. [49] Additionally, we have observed no regulation of Ostα/β, FXR target genes. These different regulatory patterns in the context of FXR activation have been observed with several ligands and might reflect the relative abundance of agonists and antagonists and co-regulatory molecules in the inflamed liver.[50]

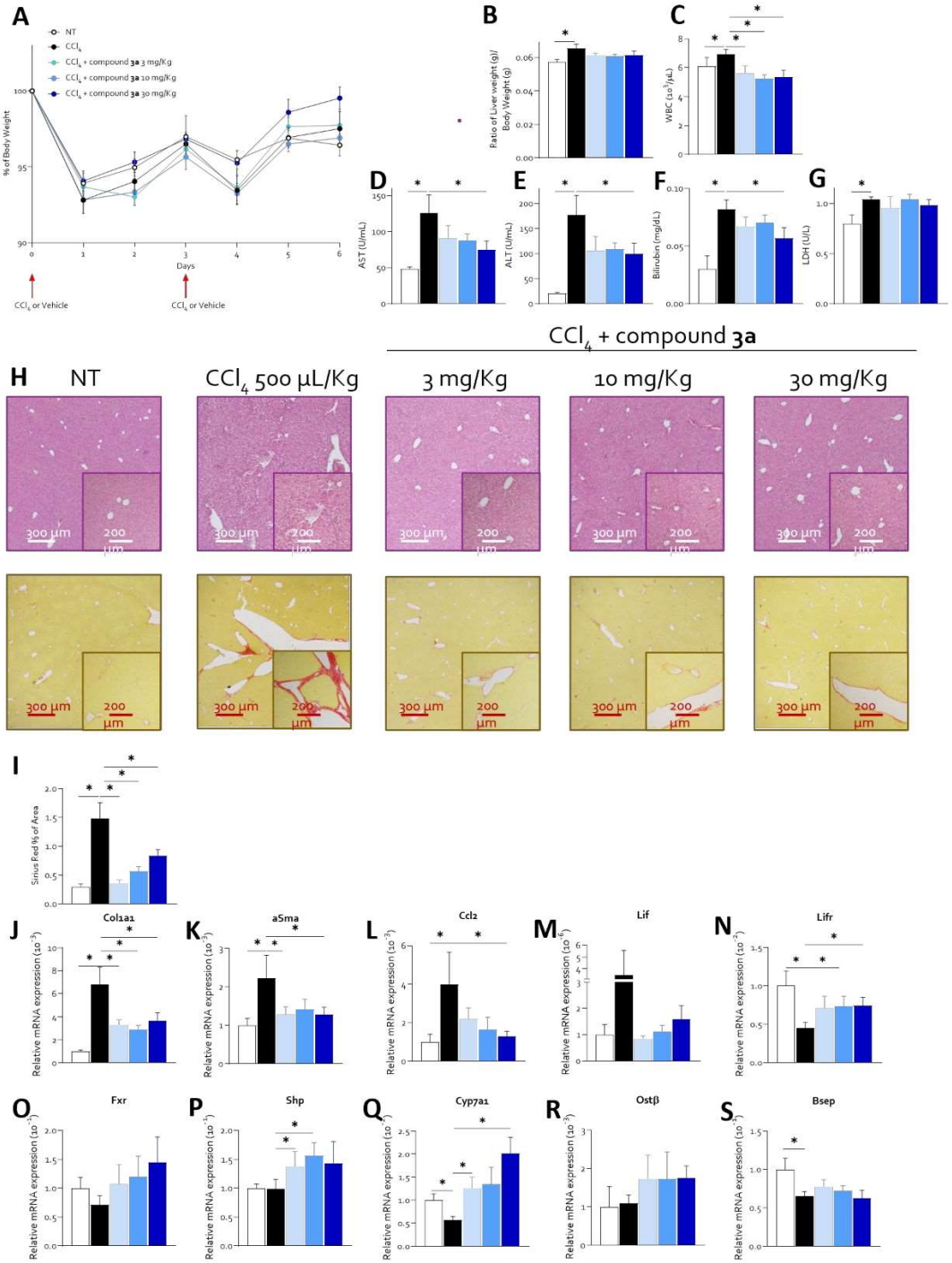

Figure 7. Compound 3a exerted a protective effect against the development of liver damage and fibrosis induced by CCl_4, improving liver function and histopathological features. In this experimental set hepatic damage was induced

in 12-week-old C57BL6/J male mice through administration of 0.5 mL/Kg CCl_4 twice a week, alone or in combination with various dosages of the compound **3a** (3-10-30 mg/Kg) for 1 weeks. The progression of the disease was monitored by recording daily body weight. (A) of % of body weight loss (B) Ratio of Liver weight and Body Weight (on left) and (C) White Blood cells ($10^3/\mu L$) in each experimental group. The severity of the disease was assessed by evaluation of (D) AST (U/mL), (E) ALT (U/mL), (F) Bilirubin (mg/dL) and (G) LDH (U/mL). (H) Haematoxylin and eosin (H&E) staining (on top) and Sirius-Red staining (on bottom) of liver section with (I) fibrosis score (% of Area). Relative mRNA expression of (J) Col1a1; (K) aSma; (L) Ccl2; (M) Lif; (N) Lifr; (O) Fxr; (P) Shp; (Q) Cyp7a1; (R) Ostβ and (S) Bsep. Each value is normalized to GAPDH. Results are the mean ± SEM of 5-8 mice per group: *p <0.05. Where not indicated, the data are not significant.

Computational studies

To elucidate the molecular basis underlying the dual activity of FXR agonism and *h*LIFR antagonism, docking and Molecular Dynamics simulations (MDs) were performed on the most promising compound of the series, compound **3a**.

Binding mode of compound 3a to FXR.

Molecular docking calculations of **3a** within the ligand binding domain (LBD) of human FXR in its active conformation (PDB ID: 3DCT)[51] revealed a top-scored docking pose similar to GW4064 (Supporting information Figure S5A), involving the key interactions typical of FXR agonists.[52,53] These include a charge-assisted H-bond of the carboxylic group with the side chain of Arg331 of Helix (H) 5, and a hydrogen bond between the isoxazole ring and the protonated His447 of H11. However, compared to the interaction of the most potent FXR agonist GW4064, we observed a sub-optimal position of the slightly shorter and more linear scaffold of **3a**, which weakens the interaction of both the carboxylic group and the isoxazole ring (Supporting information Figure S5B and S5C).

To evaluate the binding mode stability of **3a** in FXR's LBD, three independent Molecular Dynamics simulations (MDs) of 200 ns each were conducted. During the three MDs trajectories, both the receptor structure and the binding mode of **3a** (Figure 8C) were stable, resulting in a converging MDs binding mode similar to the starting docking pose (Figure 8B), characterized by interactions known to stabilize the receptor's activated conformation,[52–54] as well as those involved in the binding of bile acid derivatives to FXR.[52] In particular, the ligand's 3-(2,6-dichlorophenyl)-5-methylisoxazole moiety occupies the hydrophobic cavity of the LBD defined by helices H2, H5, H6, H7, H11, and

H12, making contacts with the residues Leu287, Thr288, Val325, Phe329, Ile352, Ile357, Met365, Tyr369, Trp454, Leu465, and Trp469 (Figure 8B). Additionally, the isoxazole ring forms a hydrogen bond with the protonated His447 of H11. The ligand's p-(phenyl)phenoxymethyl linker establishes several hydrophobic contacts with residues such as Met265, Thr270, Leu287, Met290, His294, Met328, Ser332, Ile335, and Leu348. Finally, the carboxylic group forms a charge-assisted hydrogen bond with the side chain of Arg331 of H5, which has been already reported in literature to stabilize the binding of bile acid derivatives to FXR.[52]

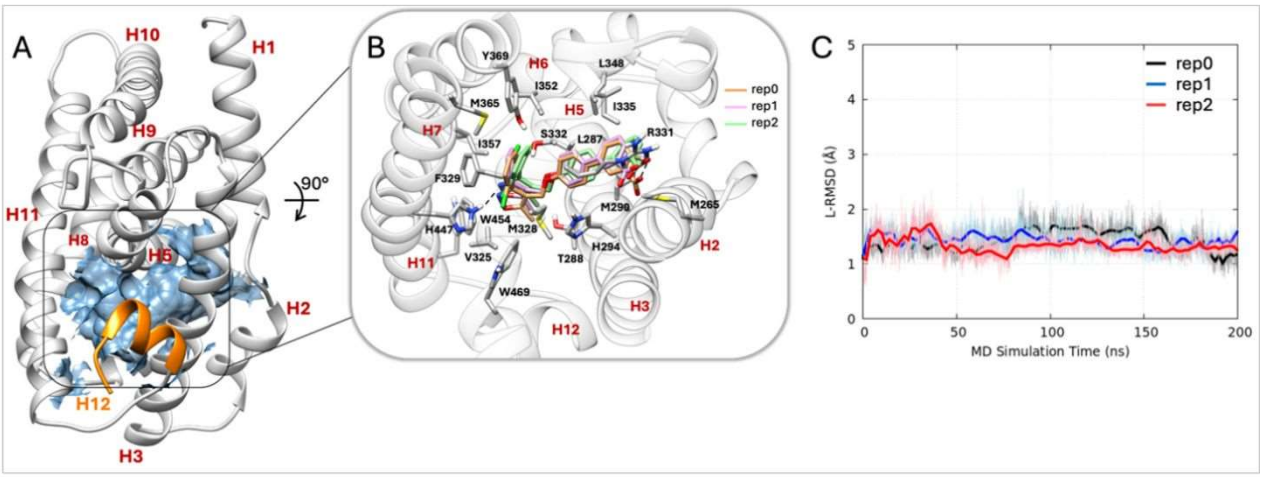

Figure 8. (A) Entire *h*FXR (PDB ID: 3DCT) used for docking calculations with definition of the ligand binding site represented in blue surface; (B) Most representative cluster (c0) of **3a** obtained after 200 ns of MDs in rep0, rep1 and rep2, represented as salmon, pink, and green stick, respectively. (C) RMSD of **3a** (L-RMSD) during 200 ns of MDs in each of the three replicas, depicting the stability of the binding mode in rep0, rep1, and rep2.

Binding mode of compound 3a to *h*LIFR. The binding mode of **3a** in *h*LIFR (PDB ID: 3E0G) (Figure 9A), was investigated using a two-step docking procedure, as successfully done in our previous works.[31,42] Compared to the FXR docking protocol, a second step of flexible docking (Induced Fit Docking; IFD) was added to take into account for the high flexibility of L1, L2 and L3 loops (Figure 9B) that defines the *h*LIFR binding site in the ligand binding process. Indeed, when protein undergoes significant conformational changes, as occurs for loops L1-L3, it is crucial to incorporate highly accurate scoring functions that consider even the receptor reorganization energy. With this approach, we selected the two best IFD poses of **3a**, named pose-A and pose-B (Supporting Information, Figure S6B and Figure S6C, respectively), characterized by a different binding mode of

the ligand because of a different L2-L3 loops arrangement. So, both pose-A and pose-B of **3a** were further investigated by means of three independent MDs replicas (namely rep0, rep1 and rep2) of 200 ns each. The overall results of the MDs replicas showed a high flexibility and consequent motion of the loops (Supporting Information, Figure S7A-D), especially of loop L3, that strongly affected the binding stability of **3a** in the *h*LIFR binding site, and more in general the shape of the binding site. As concerns the MDs of IFD pose-A, indeed, in two of the three trajectories (rep0 and rep1), the RMSD of **3a** (L-RMSD) (Figure 9C) depicted a rather stable binding behavior that converges to a very similar binding mode in the most representative MD cluster conformations (c0) retrieved from rep0 (Figure 9D) and rep1 (Figure 9E) counting respectively for the 91% and 70% of each trajectory. In both replicas, the carboxylate group is, in fact, sandwiched in electrostatic interactions between Arg330 and Lys332 in rep0 (Figure 9D) and Arg330 and Arg333 in rep1 (Figure 9E). On the other side, the dichlorophenylisoxazole moiety is caged in a flexible hydrophobic pocket lined by Trp104, Pro106, Tyr120 and Tyr144.

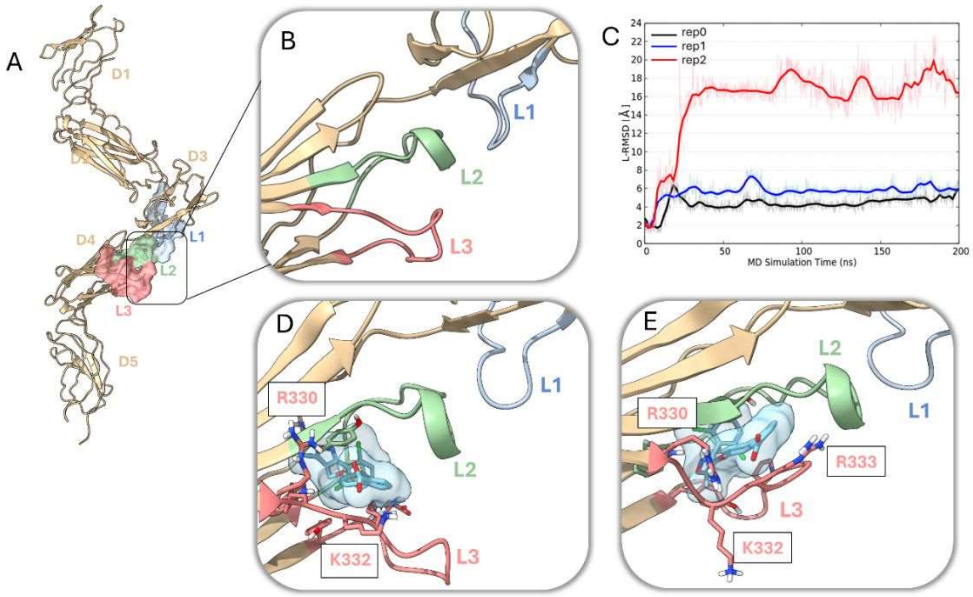

Figure 9. (A) Extracellular segment of *h*LIFR D1-D5 domains (PDB ID: 3E0G) used for docking calculations with definition of the ligand binding site defined by loop L1 (light-blue surface), L2 (green surface) and L3 (light-coral surface); (B) Focus on the L1, L2 and L3 loops defining the binding site of *h*LIFR. (C) RMSD of **3a** (L-RMSD) during 200 ns of MDs in each of the three replicas, depicting the stability of the binding mode in rep0 and rep1. (D) The most representative cluster (91%) (c0) of **3a** pose-A obtained after 200 ns of MDs in rep0; (E) The most representative cluster (70%) (c0) of **3a** pose-A obtained after 200 ns of MDs in rep1.

As concerns the MDs of IFD pose-B (Supporting Information, Figure S6C), the two most stable MDs replicas, rep0 and rep2 (Supporting Information, Figure S8A), converged to a very similar binding mode as demonstrated by the most representative MDs cluster (c0) (Supporting Information, Figure S8B and S8C, respectively). However, the population counted respectively for the 58.5% and the 57.9%, thus indicating a more variable binding mode with respect to the MDs of pose-A. Interestingly, also in both the two stable runs of pose B, the dichlorophenylisoxazole moiety established hydrophobic interactions with Trp104, Pro106, Tyr120 and Tyr144, whereas the carboxyl group is involved in salt-bridge interactions with Arg333 and one H-bond with Ser258 only in one replica.

Binding free energy calculations of **3a** were performed by means of Molecular Mechanics/Generalized Born Surface Area (MM/GBSA) and Molecular Mechanics Poisson-Boltzmann Surface Area (MM/PBSA) parameters [55] over multiple configurations of MDs snapshot belonging to each single cluster (c0-c4) (Supporting Information, Table S1) after removing the explicit solvent molecules and ions. Both MM/GBSA and MM/PBSA indicate that the pose belonging to the most representative cluster (c0) of pose-A found in rep1 (Figure 9E) is a favorable bound state towards *h*LIFR, thanks to the strong electrostatic interactions engaged by the carboxylate group of **3a** with the Arg330 and Arg333 of the L3 loop as shown by the electrostatic potential map in Supporting Information Figure S9. In such pose, in fact, the electrostatic energy gives the highest contribution to the binding, with respect to the van der Waals (-103.97 kcal/mol *vs* –53.73 kcal/mol, respectively), both in the MM/GBSA and in the MM/PBSA models, thus highlighting the importance of negatively charged group of **3a** in the binding to *h*LIFR. Furthermore, to investigate the role of the substituents at C5 position of the isoxazole ring, we have then compared the most representative pose-A of **3a** with the best IFD pose of compounds **3c** and **3e** owing the *n*-propyl and the *t*-butyl moiety, respectively. The superposition of the IFD poses highlights that, despite the biphenylcarboxylate moiety in **3c** and **3e** well overlaps that of **3a** (Supporting Information, Figure S10A and S10C,

respectively), the presence of steric substituents at C5 of the isoxazole ring induces a rotation of the isoxazole ring so that both the C5 *n*-propyl and *t*-butyl substituents point towards the loop L3 (Supporting Information, Figure S10B and S10D, respectively), giving rise to different binding modes, characterized by similar scores (Supporting Information, Table S2).

Discussion and Conclusion

In the present study, harnessing the isoxazole moiety, a well-known scaffold targeting FXR, twenty-seven new isoxazole derivatives have been prepared and tested for their activity *in vitro*. In a first cell-free screening, derivatives **1c**, **1h**, **2d**, **2e**, **2f**, **3a**, **3c**, **3e**, **4b**, and **4d** were judged excellent dual FXR agonists/LIF-LIFR antagonists. Among these ten best identified candidates, pharmacokinetics analysis, parallel artificial membrane permeability assay and *in vitro* transactivation afforded the identification of **3a** and **4d** as the most promising compounds of the series. Here on, a deeper characterization of both demonstrated that compound **3a** (EC_{50} 3.2 μM and IC_{50} 2 μM) effectively reversed macrophages and HSC activation, while promoting the expression of FXR target genes in isolated hepatocytes.

The computational study involving molecular docking followed by MDs allowed us to clarify the binding of **3a** to the human FXR and *h*LIFR receptors. The MDs of **3a** in the FXR binding pocket revealed a very stable binding, involving the key interactions typical of FXR agonists, such as a charge-assisted H-bond of the carboxylic group with the side chain of Arg331 of H5, and a hydrogen bond between the isoxazole ring and the protonated His447 of H11. In contrast, the MDs of **3a** in the antagonist binding pocket of *h*LIFR defined by loops L1, L2 and L3, was characterized by a high variability due to the high flexibility of the binding site (Supporting Information, Figure S7). Nevertheless, by analyzing the binding of **3a** across six different runs from two different IFD docking poses (pose-A and pose-B), we were able to identify some key interactions characterizing the binding of **3a**, such as the charge interaction with Arg330 or Arg333, and the hydrophobic and aromatic

interactions of the dichlorophenylisoxazole portion with residues Trp104, Pro106, Tyr120 and Tyr144.

Moreover, the results of MDs on both *h*FXR and *h*LIFR provided a molecular perspective of the observed SAR. In fact, as for position C5, in *h*FXR the methyl group of **3a** is positioned within a pocket defined by Trp227, Phe219, Phe42 and Thr46, but not fully occupy it; in contrast, the *t*-butyl substituent in **3e** fits more effectively within the pocket, maximizing hydrophobic interactions and resulting in a fivefold improvement in activity (Supporting information, Figure S5D and S5E). In contrast, in *h*LIFR the substituent at C5 pointed toward loop L3, which is very flexible (Supporting Information, Figure S7) and can well accommodate substituents of different dimensions, which aligns with the little impact on the activity observed. This evidence was also confirmed from the flexible docking (IFD) of **3c,** and **3e**, differing from **3a** in the bulkier C5 substituents, *n*-propyl and *t*-butyl, respectively. The results showed how well the compounds fit the binding site, with the biphenyl moiety binding the same area occupied in binding by **3a**, (Supporting Information, Figure S10A and S10C, respectively) but assuming different conformations depending on the size of the substituent at C5. Comparison of the docking scores shows that although different, the binding of the three compounds is comparable in terms of score (Supporting Information, Table S2).

Regarding the significant role of the disubstituted aromatic ring at C3, MDs showed no steric hindrance or potential halogen bonding in either receptor. This suggests that the impact is mainly driven by the ability of the ortho-substituents to twist the aryl group at C3 out of the plane of the isoxazole in FXR agonism, [45] thereby allowing a more favorable T-shaped interaction with Trp45. Additionally, the electronic effect on aromatic polarization could influence the aromatic interactions involving the 2,4-dichlorophenyl ring (Tyr127 and Phe201 in FXR and Tyr120 in LIFR). Finally concerning the C4 substitution, the presence of either the biphenylcarboxylate or the benzyloxybenzoate moiety works well towards both receptors, with slight variations in efficacies and potencies depending on the substitutions of biphenyl or benzyloxybenzoate moiety (e.g. **3e** *vs* **4g**, **2f**

vs **4h**, or **4d** *vs* **4f**). Consequently, we chose to maintain mostly the biphenyl group, as present in the compound **1c**, to enable easier synthetic access (fewer steps and higher yields), thus facilitating future preclinical and clinical advancements.

Finally, using HSCs, we have provided evidence that exposure to LIF promotes their activation and increases the expression of α-Sma and Col1a1, establishing a role for LIF-LIFR in hepatic stellate cells activation.[2] Together with the fact that liver LIF overexpression induces a state of cachexia, promotes the STAT3-dependent downregulation of PPARα, *de novo* lipogenesis and hepatocytes injury,[56] our findings reiterate the hypothesis that counteracting the LIF-LIFR pathway might have a translational relevance in the treatment of human disorders.

Confirming the fact that remodeling of the profibrotic microenvironment at monocytes/macrophages and hepatic stellate cell interface holds potential for *in vivo* translation, we have shown that treating CCl_4-administered mice, a model of acute fibrosis and inflammation, reverses hepatic stellate cell activation, providing a strong support for further development of compound **3a**.

These *in vivo* and *in vitro* characterizations have several limitations whose most relevant one is represented by the short duration of the CCl_4 model. Generally, severe fibrosis develops only after 6-8 weeks of treatment, while our model only lasts for 7 days. While we acknowledge this limitation, we are also confident that short models hold predictive effects in less severe forms of liver fibrosis, and more importantly allow to drive information on the macrophage-hepatic stellate cells interactions along with the modulation of inflammation-driven pathogenesis which is seen considered a druggable target in liver fibrogenesis. [57] On the other hand, hepatic stellate cells are not the unique source of ECM in liver cirrhosis, which makes it necessary to test compound **3a** in other models of liver disorders.[7]

Collectively, this study resulted in the identification of compound **3a**, a first-in-class orally active hybrid molecule acting as FXR agonist/LIFR antagonist, able to protect against the development of acute liver fibrosis and inflammation.

Experimental Section

Chemistry. High-resolution electrospray ionization mass spectrometry (ESI-MS) spectra were performed with an LTQ-XL equipped with an Ultimate 3000 HPLC system (Thermo Fisher Scientific) mass spectrometer. NMR spectra were obtained on a Bruker 400 spectrometer (^{1}H at 400, ^{13}C at 100 MHz), recorded in $CDCl_3$ (δ_H = 7.26 and δ_C = 77.0 ppm) and CD_3OD (δ_H = 3.30 and δ_C = 49.0 ppm). Detected signals were in accordance with the proposed structures. Coupling constants (*J* values) are given in hertz (Hz), and chemical shifts (δ) are reported in ppm and referred to CHD_2OD and $CHCl_3$ as internal standards. Spin multiplicities are given as s (singlet), br s (broad singlet), d (doublet), t (triplet), m (multiplet), and so on.

Preparative HPLC was performed *via*

Instrument A: Waters model 510 pump equipped with Waters® Rheodyne injector and a differential refractometer, model 401.

Instrument B: Preparative Agilent 1260 Infinity II LC system equipped with a prep binary pump G7161A (Flow rate: 25 mL/min), a Variable Wavelength Detector (VWD) G7114A detecting at 220 and 254 nM and a Fraction Collector G1364E.

Reaction progress was monitored *via* thin-layer chromatography (TLC) on Alugram silica gel G/UV254 plates. Silica gel (200–400 mesh) from Macherey-Nagel Company was used for flash chromatography. All chemicals were obtained from Merck Life Science or Zentek srl.

Flash chromatography was performed with a Biotage® Selekt, Two Channel, Single Collection Bed, UV-VIS Detector.

Solvents and reagents were used as supplied from commercial sources with the following exceptions. Hexane, ethyl acetate, chloroform, dichloromethane, tetrahydrofuran, and triethylamine were distilled from calcium hydride immediately prior to use. Methanol was dried from magnesium methoxide as follows. Magnesium turnings (5 g) and iodine (0.5 g) were refluxed in a small (50–100 mL) quantity

of methanol until all the magnesium had reacted. The mixture was diluted (up to 1 L) with reagent-grade methanol, refluxed for 2–3 h, and then distilled under nitrogen. All reactions were carried out under nitrogen atmosphere using flame-dried glassware unless stated otherwise. The purity of all compounds was assessed to be higher than 95% by ^{1}H and ^{13}C NMR.

The purity of selected compounds was further determined to be greater than 95% by analytical HPLC analysis *via* Agilent 1260 Infinity II LC system equipped with a quaternary pump VL G7111A and a Diode Array Detector WR G7115A.

Synthetic Procedures for Compounds 1b-1h

General procedure for isoxazolylmethanol intermediate (compound 5)

The corresponding isoxazole, synthesized according to the literature[44] starting from 2,6-dichlorobenzaldehyde, was dissolved in dry THF. Then, DIBAL-H (1M in THF, 3 eq) was added dropwise at 0°C. The reaction was stirred for 6 h. Upon full starting material conversion, the reaction was quenched by pouring it into a saturated solution of sodium/potassium tartrate in H_2O. After stirring for 30 min, the mixture was extracted with dichloromethane (3x10 mL). The organic phase was dried over anhydrous Na_2SO_4, filtered, and concentrated to afford the corresponding alcohol **5**.

General procedure A for the synthesis of intermediates 6 and 7 (Mitsunobu reaction)

To a solution of PPh_3 (3.5 eq) in dry THF at 0°C, DIAD (3.5 eq) was added dropwise. The suspension was stirred for 10 min, then a solution of compound **5** in dry THF was added. After 10 min, a solution of methyl 4-hydroxybenzoate or methyl 3-hydroxycarboxylate respectively in dry THF was added. After a period of 5 h, water (10 mL) was added, and the reaction mixture was evaporated at rotavapor. The residue was then extracted with EtOAc (3 x 50 mL). The combined organic layers were washed with a solution of KOH 2.5 M and water, dried and evaporated to give a yellow oil. Purification by flash chromatography (Hex/EtOAc 9:1 v/v) on silica gel gave compounds **6** and **7**.

General procedure for $LiBH_4$ reduction for intermediates 8 and 9

To a solution of compound **6** or alternatively **7** in dry THF at 0°C, dry MeOH (3 eq) was added followed by the addition of a solution of $LiBH_4$ (2M in THF, 3 eq) dropwise. The reaction was left stirring for 5 h. After starting material consumption, the reaction was quenched by adding an aqueous solution of 1M NaOH (3 eq) at 0°C and stirring for 30 min. The mixture was then extracted with EtOAc (3x10 mL). The organic phase was washed once with brine and dried over anhydrous Na_2SO_4, filtered, and concentrated. The crude was then purified by automated flash chromatography to afford the respective products **8** and **9**.

General procedure B for the synthesis of intermediates 10-14 (Williamson reaction)

Compound **5** (or compound **8** or **9**, alternatively) was dissolved in dry THF and cooled to -20°C. Then triethylamine (3 eq) was added followed by methanesulfonyl chloride (3 eq). The reaction was then left to stir for 2 h. After TLC monitoring, the mixture was diluted with distilled water and extracted with ethyl acetate (3x10 mL). The organic phase was dried over anhydrous Na_2SO_4, filtered, and concentrated to afford the corresponding methanesulphonate. To a dry DMF solution of the methanesulphonate, a suitable phenol (1.1 eq) (methyl 4-hydroxybenzoate, methyl 3-hydroxybenzoate, methyl 4'-hydroxy-[1,1'-biphenyl]-3-carboxylate, or methyl 4'-hydroxy-[1,1'-biphenyl]-4-carboxylate) and K_2CO_3 (2.5 eq) were added. The mixture was left to stir at 100°C for 6 h. Upon completion, the reaction was diluted with distilled water and extracted with EtOAc (3x10 mL). The organic phase was dried over anhydrous Na_2SO_4, filtered, and concentrated. The crude was then purified by automated flash chromatography to afford the respective products.

General procedure for basic hydrolysis

The methyl ester intermediates **10-14**, were dissolved in MeOH/H_2O 1:1 v/v and then NaOH (2 eq) was added. The reaction was stirred at reflux for 4 h. After TLC monitoring, the reaction was acidified with HCl 6 N solution and extracted with ethyl acetate (3x10 mL). dried over anhydrous Na_2SO_4, filtered, and concentrated to give the corresponding compounds **1d-1h**.

4-((4-((3-(2,6-dichlorophenyl)-5-isopropylisoxazol-4-yl)methoxy)benzyl)oxy)benzoic acid (1a), **3-((4-((3-(2,6-dichlorophenyl)-5-isopropylisoxazol-4-yl)methoxy)benzyl)oxy)benzoic acid (1b)** and **4'-((3-(2,6-dichlorophenyl)-5-isopropylisoxazol-4-yl)methoxy)-[1,1'-biphenyl]-3-carboxylic acid** (**1c**). Compounds **1a, 1b** and **1c** were obtained as stated in our previous publication.[44]

4'-((4-((3-(2,6-dichlorophenyl)-5-isopropylisoxazol-4-yl)methoxy)benzyl)oxy)-[1,1'-biphenyl]-3-carboxylic acid (1d). Purification by HPLC on a Nucleodur Sphinx C18 5 µm (4.6 mm i.d. x 250 mm) with MeOH/H_2O (95:5) and 0.1% TFA as eluent (flow rate 1 mL/min) gave compound **1d** (R_t = 5 min, 47% yield). ^{1}H NMR ($CDCl_3$, 400 MHz): δ 8.26 (s, 1H), 8.01 (d, *J* = 8.0 Hz, 1H), 7.78 (d, *J* = 8.0 Hz, 1H), 7.56 – 7.49 (m, 3H), 7.50 – 7.36 (m, 2H), 7.34 – 7.28 (m, 3H), 7.04 (d, *J* = 8.7 Hz, 2H), 6.80 (d, *J* = 8.7 Hz, 2H), 5.01 (s, 2H), 4.73 (s, 2H), 3.32 (hept, *J* = 7.0 Hz, 1H,), 1.42 (d, *J* = 7.0 Hz, 6H). ^{13}C NMR ($CDCl_3$, 100 MHz): δ 176.5, 159.3, 158.8, 158.3, 141.3, 135.9 (2C), 132.8 (2C), 131.9, 131.3 (2C), 129.6, 129.3 (2C), 129.1, 128.5 (2C), 128.4 (2C), 128.2 (2C), 128.0, 115.4 (2C), 115.0 (2C), 109.5, 69.9, 59.5, 27.2, 20.9 (2C). HR MS-ESI: for $C_{33}H_{27}Cl_2NO_5$ calculated 587.1266, found m/z 588.1302 $[M + H]^+$.

4-((3-((3-(2,6-dichlorophenyl)-5-isopropylisoxazol-4-yl)methoxy)benzyl)oxy)benzoic acid (1e). Purification by HPLC on a Nucleodur Sphinx C18 5 µm (4.6 mm i.d. x 250 mm) with MeOH/H_2O (80:20) as eluent (flow rate 1 mL/min) gave compound **1e** (R_t = 13 min, 94% yield). ^{1}H NMR ($CDCl_3$, 400 MHz): δ 8.05 (d, *J* = 8.8 Hz, 2H), 7.41 – 7.34 (m, 2H), 7.29 (dd, *J* = 8.8, 7.1 Hz, 1H), 7.23 (d, *J* = 8.2 Hz, 1H), 6.99 (d, *J* = 8.8 Hz, 3H), 6.84 (t, *J* = 2.6 Hz, 1H), 6.75 (dd, *J* = 8.2, 2.6 Hz, 1H), 5.06 (s, 2H), 4.74 (s, 2H), 3.32 (hept, *J* = 7.0 Hz, 1H), 1.41 (d, *J* = 7.0 Hz, 6H). ^{13}C NMR ($CDCl_3$, 100 MHz): δ 176.5, 163.1, 159.2, 158.7, 137.8, 135.9 (2C), 132.5 (2C), 131.3 (2C), 129.9, 128.2 (2C), 128.0, 121.8, 120.3, 114.7, 114.7 (2C), 113.8, 109.4, 70.0, 59.5, 27.2, 20.9 (2C). HR MS-ESI: for $C_{27}H_{23}Cl_2NO_5$ calculated 511.0953, found m/z 512.1027 $[M + H]^+$.

3-((3-((3-(2,6-dichlorophenyl)-5-isopropylisoxazol-4-yl)methoxy)benzyl)oxy)benzoic acid (1f). Purification by HPLC on a Nucleodur Sphinx C18 5 µm (4.6 mm i.d. x 250 mm), with MeOH/H_2O

(80:20) as eluent (flow rate 1 mL/min) gave compound **1f** (R_t 15 min, 65% yield). ^{1}H NMR ($CDCl_3$, 400 MHz) δ 7.72 (d, *J* = 7.5 Hz, 1H), 7.67 (br s, 1H), 7.41 (ovl, 1H), 7.40 (d, ovl, 2H), 7.31 (t, ovl, 1H), 7.30 (t, ovl, 1H), 7.24 (d, *J* = 8.0 Hz, 1H), 7.20 (d, *J* = 8.2 Hz, 1H), 6.87 (br s, 1H), 6.76 (d, *J* = 8.2 Hz, 1H), 5.04 (s, 2H), 4.75 (s, 2H), 3.34 (hept, *J* = 6.9 Hz, 1H), 1.42 (d, *J* = 6.9 Hz, 6H). ^{13}C NMR ($CDCl_3$, 100 MHz) δ 176.7, 165.3, 159.0, 158.9, 158.5, 137.7, 135.7 (2C), 131.3, 129.6, 129.3, 128.9, 128.4, 128.2 (2C), 120.9, 120.5, 116.1, 115.3, 114.7, 113.8, 110.1, 69.6, 59.3, 27.0, 20.5 (2C). HR MS-ESI: for $C_{27}H_{23}Cl_2NO_5$ calculated 511.0953, found m/z 512.1031 $[M + H]^+$.

4'-((3-((3-(2,6-dichlorophenyl)-5-isopropylisoxazol-4-yl)methoxy)benzyl)oxy)-[1,1'-biphenyl]-3-carboxylic acid (1g). Purification by HPLC on a Phenomenex C18 5 μm (4.6 mm i.d. x 250 mm), with MeOH/H_2O (80:20) as eluent (flow rate 1 mL/min) gave compound **1g** (R_t = 11 min, 44% yield). ^{1}H NMR (CD_3OD, 400 MHz) δ 8.27 (br s, 1H) 8.02 (d, *J* = 7.8 Hz, 1H), 7.75 (d, *J* = 7.8 Hz, 1H), 7.56 (d, *J* = 8.2 Hz, 2H), 7.52 (t, *J* = 7.8 Hz, 1H), 7.40 (d, *J* = 8.0 Hz, 2H), 7.32 (t, *J* = 8.0 Hz, 1H), 7.30 (t, *J* = 7.5 Hz, 1H), 7.04 (d, *J* = 8.2 Hz, 2H), 7.00 (d, *J* = 7.5 Hz, 1H), 6.85 (s, 1H), 6.80 (d, *J* = 7.5 Hz, 1H), 5.06 (s, 2H), 4.78 (s, 2H), 3.33 (hept, *J* = 7.3 Hz, 1H), 1.42 (d, *J* = 7.3 Hz, 6H). ^{13}C NMR ($CDCl_3$, 100 MHz): δ 176.4, 165.5, 159.1, 158.7, 158.5, 141.0, 137.7, 135.6 (2C), 132.3, 131.8, 131.6, 131.4, 129.8, 129.5, 129.1, 128.9, 128.4 (2C), 128.2 (2C), 127.6, 120.4, 115.1 (2C), 114.5, 113.7, 109.3, 69.8, 59.3, 27.0, 20.7 (2C). HR MS-ESI: for $C_{33}H_{27}Cl_2NO_5$ calculated 587.1266, found m/z 588.1382 $[M + H]^+$.

4'-((3-(2,6-dichlorophenyl)-5-isopropylisoxazol-4-yl)methoxy)-[1,1'-biphenyl]-4-carboxylic acid (1h). The hydrolysis crude was purified by preparative HPLC employing an Agilent Pre-C18 column (30x100 mm, 5 μm) with solvent A (water 0.1% TFA) and B (ACN 0.1% TFA) in a linear gradient from 60% B to 95% B in 20 min to afford compound **1h** (R_t = 9.72 min, 77% yield). ^{1}H NMR ($CDCl_3$, 400 MHz): δ 8.14 (d, *J* = 8.5 Hz, 2H), 7.61 (d, *J* = 8.5 Hz, 2H), 7.51 (d, *J* = 8.8 Hz, 2H), 7.45 – 7.38 (m, 2H), 7.32 (dd, *J* = 9.0, 7.1 Hz, 1H), 6.88 (d, *J* = 8.8 Hz, 1H), 4.78 (s, 2H), 3.35 (hept, *J* = 7.0 Hz, 1H), 1.44 (d, *J* = 7.0 Hz, 6H). ^{13}C NMR ($CDCl_3$, 100 MHz) δ 176.6, 171.6, 159.2,

158.7, 146.0, 135.9 (2C), 133.0, 131.4, 130.9 (2C), 128.5 (2C), 128.3 (2C), 127.9, 127.5, 126.7 (2C), 115.3 (2C), 109.4, 59.6, 27.28, 20.9 (2C). HR MS-ESI: for $C_{26}H_{21}Cl_2NO_4$ calculated 481.3570, found *m/z* 480.0848 $[M - H]^-$.

Synthetic Procedures for Compounds 2a-2h

The synthetic protocols for intermediates **15-19,** and **26** were the same employed for compound **5**, with a different starting material (2-bromobenzaldehyde, 2-chlorobenzaldehyde, 2-trifluoromethylbenzaldehyde, 2,6-dibromobenzaldehyde, 2-bromo-6-chlorobenzaldehyde, 2,4-dichlorobenzaldehyde), Then, **15-19** and **26** were coupled to methyl 4'-hydroxy-[1,1'-biphenyl]-3-carboxylate with a Mitsunobu reaction (see Procedure A), providing compounds **20-24** and **27**, which were subjected to a subsequent basic hydrolysis. **19** and **28** were coupled to methyl 4'-hydroxy-[1,1'-biphenyl]-4-carboxylate and methyl 4-hydroxybenzoate respectively *via* Williamson reaction (see Procedure B) to achieve **25** and **29**, subsequently hydrolyzed in basic conditions.

4'-((3-(2-bromophenyl)-5-isopropylisoxazol-4-yl)methoxy)-[1,1'-biphenyl]-3-carboxylic acid (2a). The hydrolysis crude was purified by HPLC employing a Nucleodur Sphinx RP column (5 µm) with 80% MeOH as eluent (flow rate 3 mL/min) to afford compound **2a** (R_t = 12.8 min, 90% yield). ^{1}H NMR ($CDCl_3$, 400 MHz): δ 8.26 (s, 1H), 8.04 (d, *J* = 7.8 Hz, 1H), 7.75 (d, *J* = 7.8 Hz, 1H), 7.68 (dd, *J* = 7.9, 1.3 Hz, 1H), 7.55 – 7.48 (m, 2H), 7.51 – 7.36 (m, 3H), 7.33 (td, *J* = 7.7, 2.0 Hz, 1H), 6.87 (d, *J* = 8.8 Hz, 2H), 4.84 (s, 2H), 3.34 (hept, *J* = 7.0 Hz, 1H), 1.43 (d, *J* = 7.0 Hz, 6H).^{13}C NMR ($CDCl_3$, 100 MHz): δ 176.8, 162.7, 157.9 (2C), 140.6, 133.7, 133.1 (2C), 132.0 (2C), 131.2 (2C), 130.5, 128.7, 128.3 (2C), 127.6 (2C), 123.2, 115.3 (2C), 109.3, 59.8, 27.2, 20.8 (2C). HR MS-ESI: for $C_{26}H_{22}BrNO_4$ calculated 491.0732, found *m/z* 492.0810 $[M + H]^+$.

4'-((3-(2-chlorophenyl)-5-isopropylisoxazol-4-yl)methoxy)-[1,1'-biphenyl]-3-carboxylic acid (2b). The hydrolysis crude was purified by HPLC employing a Nucleodur Sphinx RP column (5 µm) with 80% MeOH as eluent (flow rate 3 mL/min) to afford compound **2b** (R_t = 13 min, 53% yield).

^{1}H NMR (DMSO-d6, 400 MHz) δ 13.04 (1H, br s, COO**H**), 8.09 (t, *J* = 1.8 Hz, 1H), 7.94 – 7.85 (m, 1H), 7.83 (dt, *J* = 8.1, 1.3 Hz, 1H), 7.63 (dd, *J* = 8.1, 1.3 Hz, 1H), 7.60 – 7.38 (m, 6H), 6.92 (d, *J* = 8.8 Hz, 2H), 4.90 (s, 2H), 3.44 (hept, *J* = 7.0 Hz, 1H), 1.34 (d, *J* = 7.0 Hz, 6H). ^{13}C NMR (DMSO-d6, 100 MHz): δ 176.0, 167.3, 160.9, 157.7, 140.0, 132.4, 132.2, 131.7 (2C), 131.5, 130.6, 129.8, 129.2, 127.8 (2C), 127.8, 127.6, 127.4, 126.8, 115.4 (2C), 109.4, 59.1, 26.0, 20.6 (2C). HR MS-ESI: for $C_{26}H_{22}ClNO_4$ calculated 447.9150, found *m/z* 448.1311 $[M + H]^+$.

4'-((5-isopropyl-3-(2-(trifluoromethyl)phenyl)isoxazol-4-yl)methoxy)-[1,1'-biphenyl]-3-carboxylic acid (2c). The hydrolysis crude was then purified by HPLC employing a Nucleodur Sphinx RP column (5 µm) with 80% MeOH as eluent (flow rate 3 mL/min) to afford compound **2c** (R_t = 12 min, 46% yield). ^{1}H NMR ($CDCl_3$, 400 MHz): δ 8.24 (s, 1H), 8.02 (d, *J* = 7.8 Hz, 1H), 7.83 – 7.72 (m, 2H), 7.51 (dd, *J* = 8.4, 6.9 Hz, 4H), 6.87 (d, *J* = 8.8 Hz, 1H), 4.71 (s, 2H), 3.33 (hept, *J* = 7.0 Hz, 1H), 1.43 (d, *J* = 7.0, 6H). ^{13}C NMR ($CDCl_3$, 100 MHz): δ 176.6, 171.1, 161.5, 158.3, 141.1, 135.4 (**C**-F_3, q, J^{13}C-^{19}F), 133.3 (**C**-F_3, q, J^{13}C-^{19}F), 132.2, 132.1, 132.0, 131.7 (**C**-F_3, q, J^{13}C-^{19}F), 130.2 (**C**-F_3, q, J^{13}C-^{19}F), 129.8, 129.8 (2C), 129.1, 128.6, 128.5, 128.4 (2C), 127.5, 126.7 (**C**$_{Ar}$-CF_3, q), 125.2, 115.3 (2C), 109.5, 59.3, 29.8, 20.9 (2C). ^{19}F NMR ($CDCl_3$, 376 MHz): δ -58.60 (C**F$_3$**). HR MS-ESI: for $C_{27}H_{22}F_3NO_4$ calculated 481.1501, found *m/z* 482.1574 $[M + H]^+$.

4'-((3-(2,6-dibromophenyl)-5-isopropylisoxazol-4-yl)methoxy)-[1,1'-biphenyl]-3-carboxylic acid (2d). The hydrolysis crude was purified by preparative HPLC employing an Agilent Pre-C18 column (30x100 mm, 5 µm) with solvent A (water 0.1% TFA) and B (ACN 0.1% TFA) in a linear gradient from 70% B to 95% B in 15 min to afford compound **2d** (R_t = 7.26 min, 58% yield). ^{1}H NMR ($CDCl_3$, 400 MHz): δ 8.24 (t, *J* = 1.7 Hz, 1H), 8.02 (dt, *J* = 7.8, 1.4 Hz, 1H), 7.79 – 7.72 (m, 1H), 7.63 (d, *J* = 8.0 Hz, 2H), 7.55 – 7.46 (m, 3H), 7.17 (t, *J* = 8.1 Hz, 1H), 6.89 (d, *J* = 8.8 Hz, 2H), 4.78 (s, 2H), 3.36 (hept, *J* = 7.0 Hz, 1H), 1.44 (d, *J* = 7.0 Hz, 6H). ^{13}C NMR ($CDCl_3$, 100 MHz): δ 176.6, 162.3, 158.4, 141.2, 133.1, 132.0 (2C), 132.0 (2C), 131.7, 129.7, 129.1 (2C), 128.6, 128.5,

128.3 (2C), 125.1 (2C), 115.3 (2C), 109.0, 59.6, 27.3, 20.9 (2C). HR MS-ESI: for $C_{26}H_{21}Br_2NO_4$ calculated 568.9837, found *m/z* 571.9890 $[(M+2) + H]^+$.

4'-((3-(2-bromo-6-chlorophenyl)-5-isopropylisoxazol-4-yl)methoxy)-[1,1'-biphenyl]-3-carboxylic acid (2e). The hydrolysis crude was purified by HPLC employing a Nucleodur Sphinx RP column (5 µm) with 80% MeOH as eluent (flow rate 3 mL/min) to afford compound **2e** (R_t = 15.5 min, 98% yield). ^{1}H NMR ($CDCl_3$, 400 MHz): δ 8.22 (s, 1H), 7.98 (s, 1H), 7.70 (s, 1H), 7.57 (d, *J* = 8.1 Hz, 1H), 7.43 (d, *J* = 9.1 Hz, 4H), 7.22 (d, *J* = 8.0 Hz, 1H), 6.84 (s, 2H), 4.75 (s, 2H), 3.38 – 3.30 (m, 1H), 1.42 (d, *J* = 7.0 Hz, 6H). ^{13}C NMR ($CDCl_3$, 100 MHz): δ 176.6, 171.9, 160.8, 158.3, 141.1, 135.8, 133.2, 132.0, 131.7, 131.4, 129.8, 129.5, 129.1, 128.8, 128.6, 128.5, 128.4, 128.3 (2C), 115.3 (2C), 109.3, 59.6, 27.3, 20.9 (2C). HR MS-ESI: for $C_{26}H_{21}BrClNO_4$ calculated 525.0342, found *m/z* 526.0416 $[M + H]^+$.

4'-((3-(2-bromo-6-chlorophenyl)-5-isopropylisoxazol-4-yl)methoxy)-[1,1'-biphenyl]-4-carboxylic acid (2f). The hydrolysis crude was purified by preparative HPLC employing an Agilent Pre-C18 column (30x100 mm, 5 µm) with solvent A (water 0.1% TFA) and B (ACN 0.1% TFA) in a linear gradient from 60% B to 95% B in 15 min to afford compound **2f** (R_t = 11.18 min, 73% yield). ^{1}H NMR ($CDCl_3$, 400 MHz): δ 8.13 (d, *J* = 8.5 Hz, 2H), 7.62 (d, *J* = 8.5 Hz, 2H), 7.59 (dd, *J* = 8.1, 1.1 Hz, 1H), 7.51 (d, *J* = 8.7 Hz, 2H), 7.45 (dd, *J* = 8.1, 1.1 Hz, 1H), 7.25 (t, *J* = 8.1 Hz, 1H), 6.89 (d, *J* = 8.8 Hz, 2H), 4.78 (s, 2H), 3.35 (hept, *J* = 7.0 Hz, 1H), 1.44 (d, *J* = 7.0 Hz, 6H).^{13}C NMR ($CDCl_3$, 100 MHz): δ 176.6, 170.5, 160.7, 158.7, 145.9, 135.8, 133.0, 131.7 (2C), 131.4, 130.8 (2C), 129.8, 128.8, 128.5 (2C), 127.6, 126.7 (2C), 125.2, 115.3 (2C), 109.2, 59.6, 27.2, 20.9, 20.9. HR MS-ESI: for $C_{26}H_{21}BrClNO_4$ calculated 525.0432, found *m/z* 524.0321 $[M - H]^-$.

4'-((3-(2,4-dichlorophenyl)-5-isopropylisoxazol-4-yl)methoxy)-[1,1'-biphenyl]-3-carboxylic acid (2g). The hydrolysis crude was purified by HPLC employing a Nucleodur Sphinx RP column (5 µm) with 80% MeOH as eluent (flow rate 3 mL/min) to afford compound **2g** (R_t = 24 min, 90% yield). ^{1}H NMR ($CDCl_3$, 400 MHz) δ 7.88 (s, 1H), 7.73 (d, *J* = 8.0 Hz, 1H), 7.56 (m, 2H), 7.48 (s,

1H), 7.43 (d, *J* = 8.0 Hz, 1H), 7.40 (d, *J* = 9.0 Hz, 1H), 7.09 (d, *J* = 8.3 Hz, 2H), 6.58 (d, *J* = 8.3 Hz, 2H), 5.60 (s, 2H), 3.10 (hept, *J* = 7.3 Hz, 1H), 1.34 (d, *J* = 7.3 Hz, 6H). ^{13}C NMR ($CDCl_3$, 100 MHz) δ 176.9, 162.5, 158.1, 140.6, 134.0, 133.0, 132.0 (2C), 131.3 (2C), 130.4 (2C), 129.0, 128.4, 128.2 (2C), 127.4 (2C), 123.1, 115.2 (2C), 109.32, 59.7, 27.3, 20.9 (2C). HR MS-ESI: for $C_{26}H_{21}Cl_2NO_4$ calculated 481.0848, found *m/z* 482.0974 $[M + H]^+$.

4-((4-((3-(2,4-dichlorophenyl)-5-isopropylisoxazol-4-yl)methoxy)benzyl)oxy)benzoic acid (2h). The hydrolysis crude was purified by HPLC employing a Nucleodur Sphinx RP column (5 µm) with 80% MeOH as eluent (flow rate 3 mL/min) to afford compound **2h** (R_t = 24.2 min, 90% yield). ^{1}H NMR ($CDCl_3$, 400 MHz) δ 8.02 (d, *J* = 7.8 Hz, 2H), 7.50 (d, J_{para} = 1.8 Hz, 1H), 7.39 (d, *J* = 8.4 Hz, 2H), 7.32-7.30 (ovl, 3H), 6.98 (d, *J* = 7.8 Hz, 2H), 6.80 (d, *J* = 8.4 Hz, 2H), 5.03 (s, 2H), 4.77 (s, 2H), 3.30 (hept, *J* = 7.0 Hz, 1H), 1.40 (d, *J* = 7.0 Hz, 6H). ^{13}C NMR ($CDCl_3$, 100 MHz): δ 177.0, 163.1 160.6, 158.3, 136.6, 134.5, 135.2 (2C), 132.5, 130.0 (2C), 129.4 (2C), 129.1, 127.5 (2C), 127.1, 115.1 (2C), 114.7 (2C), 109.3, 70.0, 59.6, 27.2, 20.9 (2C). HR MS-ESI: for $_{27}H_{23}Cl_2NO_5$ calculated 511.0953, found *m/z* 512.1002 $[M + H]^+$.

Synthetic Procedures for Compounds 3a-3e

The intermediates **30-34** were synthesized according to the synthetic protocol of compound **5**, using 2,6-dichlorobenzaldehyde as starting material and five different β-ketoesters (methyl 3-oxobutanoate, methyl 4-methoxy-3-oxobutanoate, methyl 3-oxohexanoate, methyl 3-oxoheptanoate, and methyl 4,4-dimethyl-3-oxopentanoate, respectively). Then, **30-34** were coupled to methyl 4'-hydroxy-[1,1'-biphenyl]-3-carboxylate with a Mitsunobu reaction (see Procedure A), providing compounds **35-39**, which were subjected to a subsequent basic hydrolysis.

4'-((3-(2,6-dichlorophenyl)-5-methylisoxazol-4-yl)methoxy)-[1,1'-biphenyl]-3-carboxylic acid (3a). The hydrolysis crude was purified by HPLC employing a Phenomenex Luna C18 column (4.6x250 mm, 5 µm) with solvent A (water 0.1% TFA) and B (ACN 0.1% TFA) in a linear gradient from 40% B to 95% B in 10 min (flow rate 1.5 mL/min) to afford compound **3a** (R_t = 13.3 min, 95%

yield). ^{1}H NMR ($CDCl_3$, 400 MHz): δ 8.27 (s, 1H), 8.04 (d, *J* = 7.7 Hz, 1H), 7.77 (d, *J* = 7.7 Hz, 1H), 7.51 (d, *J* = 8.2 Hz, 2H), 7.53 (t, *J* = 7.7 Hz, 1H), 7.43 (d, *J* = 8.0 Hz, 2H), 7.34 (t, *J* = 8.0 Hz, 1H), 6.89 (d, *J* = 8.2 Hz, 2H), 4.80 (s, 2H), 2.59 (s, 3H). ^{13}C NMR ($CDCl_3$, 100 MHz): δ 168.6, 165.4, 159.0, 158.1, 141.0, 135.8 (2C), 133.1, 131.8 (2C), 131.3, 129.0, 128.5, 128.4, 128.2 (2C), 128.1 (2C), 127.8, 115.1 (2C), 111.2, 59.7, 11.6. HR MS-ESI: for $C_{24}H_{17}Cl_2NO_4$ calculated 453.0535, found *m/z* 454.0608 $[M + H]^+$.

4'-((3-(2,6-dichlorophenyl)-5-(methoxymethyl)isoxazol-4-yl)methoxy)-[1,1'-biphenyl]-3-carboxylic acid (3b). The hydrolysis crude was purified by HPLC employing a Phenomenex Luna C18 column (4.6x250 mm, 5 µm) with solvent A (water 0.1% TFA) and B (ACN 0.1% TFA) in a linear gradient from 40% B to 95% B in 10 min (flow rate 1.5 mL/min) to afford compound **3b** (R_t = 15.5 min, 90% yield). ^{1}H NMR ($CDCl_3$, 400 MHz): δ 8.27 (s, 1H), 8.04 (d, *J* = 7.7 Hz, 1H), 7.77 (d, *J* = 7.7 Hz, 1H), 7.51 (d, *J* = 8.5 Hz, 2H), 7.50 (t, *J* = 7.7 Hz, 1H), 7.42 (d, *J* = 8.0 Hz, 2H), 7.35 (t, *J* = 8.0 Hz, 1H), 6.87 (d, *J* = 8.5 Hz, 2H), 4.93 (s, 2H), 4.78 (s, 2H), 3.50 (s, 3H). ^{13}C NMR ($CDCl_3$, 100 MHz): δ 171.2, 167.1, 159.2, 158.0, 140.9, 135.8 (2C), 133.1, 131.8, 131.4 (2C), 128.9, 128.3, 128.2 (2C), 128.1 (4C), 115.1 (2C), 113.8, 64.6, 59.2, 58.9. HR MS-ESI: for $C_{25}H_{19}Cl_2NO_5$ calculated 483.0640, found *m/z* 484.0714 $[M + H]^+$.

4'-((3-(2,6-dichlorophenyl)-5-propylisoxazol-4-yl)methoxy)-[1,1'-biphenyl]-3-carboxylic acid (3c). The hydrolysis crude was purified by HPLC employing a Phenomenex Luna C18 column (4.6x250 mm, 5 µm) with solvent A (water 0.1% TFA) and B (ACN 0.1% TFA) in a linear gradient from 40% B to 95% B in 10 min (flow rate 1.5 mL/min) to afford compound **3c** (R_t = 14.8 min, 88% yield). ^{1}H NMR ($CDCl_3$, 400 MHz): δ 8.26 (s, 1H), 8.04 (d, *J* = 7.8 Hz, 1H), 7.76 (d, *J* = 7.8 Hz, 1H), 7.50 (d, *J* = 8.5 Hz, 2H), 7.52 (t, *J* = 7.8 Hz, 1H), 7.42 (d, *J* = 8.0 Hz, 2H), 7.34 (t, *J* = 8.0 Hz, 1H), 6.88 (d, *J* = 8.5 Hz, 2H), 4.78 (s, 2H), 2.91 (t, *J* = 7.3 Hz, 2H), 1.86 (sext, *J* = 7.3 Hz, 2H), 1.04 (t, *J* = 7.3 Hz, 3H); ^{13}C NMR ($CDCl_3$, 100 MHz): δ 172.2, 165.2, 159.0, 158.1, 141.0, 135.8 (2C), 133.0,

131.9, 131.3 (2C), 129.0, 128.5, 128.4, 128.2 (2C), 128.1 (2C), 127.9, 115.1 (2C), 111.0, 59.5, 27.9, 21.1, 13.6. HR MS-ESI: for $C_{26}H_{21}Cl_2NO_{44}$ calculated 481.0848 found *m/z* 482.0921 $[M + H]^+$.

4'-((5-butyl-3-(2,6-dichlorophenyl)isoxazol-4-yl)methoxy)-[1,1'-biphenyl]-3-carboxylic acid (3d). The hydrolysis crude was purified by HPLC employing a Phenomenex Luna C18 column (4.6x250 mm, 5 µm) with solvent A (water 0.1% TFA) and B (ACN 0.1% TFA) in a linear gradient from 40% B to 95% B in 10 min (flow rate 1.5 mL/min) to afford compound **3d** (R_t = 15.7 min, 88% yield). ^{1}H NMR ($CDCl_3$, 400 MHz): δ 8.27 (s, 1H), 8.05 (d, *J* = 7.8 Hz, 1H), 7.76 (d, *J* = 7.8 Hz, 1H), 7.52 (t, *J* = 7.8 Hz, 1H), 7.50 (d, *J* = 8.6 Hz, 2H), 7.42 (d, *J* = 8.0 Hz, 2H), 7.34 (t, *J* = 8.0 Hz, 1H), 6.88 (d, *J* = 8.6 Hz, 2H), 4.78 (s, 2H), 2.93 (t, *J* = 7.3 Hz, 2H), 1.81 (quint, *J* = 7.3 Hz, 2H), 1.44 (h, *J* = 7.3 Hz, 2H), 0.98 (t, *J* = 7.3 Hz, 3H). ^{13}C NMR ($CDCl_3$, 100 MHz): δ 172.4, 170.5, 159.0, 158.1, 141.0, 135.8 (2C), 133.1, 131.7, 131.3 (2C), 128.9, 128.4, 128.3, 128.2 (2C), 128.1 (2C), 127.8, 115.2 (2C), 110.8, 59.6, 29.6, 25.7, 22.2, 13.7. HR MS-ESI: for $C_{27}H_{23}Cl_2NO_4$ calculated 495.1004, found *m/z* 496.1077 $[M + H]^+$.

4'-((5-(tert-butyl)-3-(2,6-dichlorophenyl)isoxazol-4-yl)methoxy)-[1,1'-biphenyl]-3-carboxylic acid (3e). The hydrolysis crude was purified by HPLC employing a Phenomenex Luna C18 column (4.6x250 mm, 5 µm) with solvent A (water 0.1% TFA) and B (ACN 0.1% TFA) in a linear gradient from 40% B to 95% B in 10 min (flow rate 1.5 mL/min) to afford compound **3e** (R_t = 18.3 min, 70% yield). ^{1}H NMR ($CDCl_3$, 400 MHz): δ 8.28 – 8.25 (m, 1H), 8.07 – 8.02 (m, 1H), 7.76 (d, *J* = 7.8 Hz, 1H), 7.54 – 7.47 (m, 3H), 7.40 (dd, *J* = 8.0, 1.9 Hz, 2H), 7.32 (ddd, *J* = 8.5, 7.4, 2.0 Hz, 1H), 6.89 – 6.84 (m, 2H), 4.77 (d, *J* = 2.4 Hz, 2H), 1.53 (d, *J* = 2.4 Hz, 9H). ^{13}C NMR ($CDCl_3$, 100 MHz): δ 178.5, 172.6, 160.1, 158.1, 140.9, 135.9 (2C), 132.9, 131.6, 131.2 (2C), 128.8, 128.3, 128.2 (2C), 128.1 (3C), 127.9, 115.0 (2C), 108.9, 59.5, 34.5, 28.9 (3C). HR MS-ESI: for $C_{27}H_{23}Cl_2NO_4$ calculated 494.1004, found *m/z* 493.1501 $[M - H]^-$.

Synthetic Procedures for Compounds 4a-4i

The compounds **40-42** were synthesized according to the synthetic protocol previously described for the synthesis of compound **5**, using three different benzaldehydes as starting material (2-chlorobenzaldehyde, 2,6-dibromobenzaldehyde, 2-bromo-6-chlorobenzaldehyde) and methyl 4,4-dimethyl-3-oxopentanoate as β-ketoester. Then, compounds **40-42** were coupled to methyl 4'-hydroxy-[1,1'-biphenyl]-3-carboxylate with a Mitsunobu reaction (see Procedure A), providing compounds **43-45**, which were subjected to a subsequent basic hydrolysis.

Starting from 2,6-dichlorobenzaldehyde and 2-bromo-6-chlorobenzaldehyde, we obtained compounds **46** and **47**, that were coupled to methyl 4'-hydroxy-[1,1'-biphenyl]-4-carboxylate with a Williamson reaction (see Procedure B), providing intermediates **48** and **49**. Alternatively compounds **46** and **47** were coupled with methyl 4-hydroxybenzoate with Mitsunobu reaction (see Procedure A), furnishing compounds **50** and **52**, that were subjected to $LiBH_4$ reduction. Alcohols **51** and **53** were subjected to Williamson reaction (see Procedure B), furnishing compounds **54-57**. All intermediates (compounds **43-45**, **48**, **49**, **54-57**) were subjected to a basic hydrolysis.

4'-((5-(tert-butyl)-3-(2-chlorophenyl)isoxazol-4-yl)methoxy)-[1,1'-biphenyl]-3-carboxylic acid (4a). The hydrolysis crude was purified by HPLC employing a Nucleodur Sphinx RP column (5 μm) with 80% MeOH as eluent (flow rate 3 mL/min) to afford compound **4a** (R_t = 23 min, 86% yield). ^{1}H NMR ($CDCl_3$, 400 MHz): δ 8.24 (s, 1H), 8.01 (d, *J* = 7.8 Hz, 1H), 7.74 (d, *J* = 7.9 Hz, 1H), 7.47 (m, 5H), 7.40 (t, *J* = 7.3 Hz, 1H), 7.33 (t, *J* = 7.5 Hz, 1H), 6.87 (d, *J* = 8.2 Hz, 2H), 4.82 (s, 2H), 1.52 (s, 9H). ^{13}C NMR ($CDCl_3$, 100 MHz): δ 176.7, 161.1, 157.7, 140.1, 133.5 (2C), 133.2, 131.9, 131.8 (2C), 131.0, 129.9, 129.8 (2C), 128.3, 127.9 (2C), 127.0 (2C), 115.00 (2C), 109.3, 59.6, 27.1, 20.8 (3C). HR MS-ESI: for $C_{27}H_{24}ClNO_4$ calculated 461.1394, found *m/z* 462.1467 $[M + H]^+$.

4'-((5-(tert-butyl)-3-(2,6-dibromophenyl)isoxazol-4-yl)methoxy)-[1,1'-biphenyl]-3-carboxylic acid (4b). The hydrolysis crude was purified by preparative HPLC employing an Agilent Pre-C18 column (30x100 mm, 5 μm) with solvent A (water 0.1% TFA) and B (ACN 0.1% TFA) in a linear gradient from 70% B to 95% B in 15 min to afford compound **4b** (R_t = 8.6 min, 86% yield). ^{1}H NMR

(MeOD, 400 MHz): δ 8.18 (s, 1H), 7.93 (d, *J* = 7.8 Hz, 1H), 7.75 (ovl, 1H), 7.72 (d, *J* = 8.1 Hz, 2H), 7.51 (d, *J* = 8.7 Hz, 2H), 7.48 (ovl, 1H), 7.28 (t, *J* = 8.1 Hz, 1H), 6.88 (d, *J* = 8.8 Hz, 2H), 4.83 (s, 2H), 1.53 (s, 9H). ^{13}C NMR (MeOD, 100 MHz): δ 178.7, 163.6, 163.3, 158.3, 141.2, 133.1, 132.0 (2C), 131.9 (2C), 131.7 (2C), 129.0, 128.5, 128.4, 128.3 (2C), 125.2 (2C), 115.1 (2C), 108.7, 59.7, 34.7, 29.0 (3C). HR MS-ESI: for $C_{27}H_{23}Br_2NO_4$ calculated 582.9994, found *m/z* 586.0047 [(M+2) + H]$^+$.

4'-((3-(2-bromo-6-chlorophenyl)-5-(tert-butyl)isoxazol-4-yl)methoxy)-[1,1'-biphenyl]-3-carboxylic acid (4c). The hydrolysis crude was purified by HPLC employing a Nucleodur Sphinx RP column (5 µm) with 80% MeOH as eluent (flow rate 1.0 mL/min) to afford **4c** (R_t = 10.5 min, 80% yield). ^{1}H NMR (400 MHz, DMSO-d6): δ 13.03 (1H, br s, COO**H**), 8.09 (s, 1H), 7.87 (d, *J* = 7.8 Hz, 1H), 7.80 (ovl, 1H), 7.77 (d, *J* = 8.1 Hz, 1H), 7.66 (d, *J* = 8.1 Hz, 1H), 7.61 – 7.50 (m, 3H), 7.46 (t, *J* = 8.1 Hz, 1H), 6.92 (d, *J* = 8.8 Hz, 2H), 4.83 (dd, *J* = 12.1, 3.5 Hz, 2H), 1.47 (s, 9H). ^{13}C NMR (100 MHz, DMSO-d6): δ 177.7, 161.3, 157.7, 134.6 (2C), 132.7, 131.5 (2C), 131.5, 129.1, 128.9, 128.8 (2C), 127.9 (2C), 127.6 (2C), 126.8, 124.5, 115.0 (2C), 108.9, 59.3, 34.0, 28.4 (3C). HR MS-ESI: for $C_{27}H_{23}BrClNO_4$ calculated 539.0499, found *m/z* 540.0572 [M + H]$^+$.

4'-((5-(tert-butyl)-3-(2,6-dichlorophenyl)isoxazol-4-yl)methoxy)-[1,1'-biphenyl]-4-carboxylic acid (4d). The hydrolysis crude was purified by preparative HPLC employing an Agilent Pre-C18 column (30x100 mm, 5 µm) with solvent A (water 0.1% TFA) and B (ACN 0.1% TFA) in a linear gradient from 60% B to 95% B in 15 min to afford **4d** (R_t = 12.4 min, 95% yield). ^{1}H NMR ($CDCl_3$, 400 MHz): δ 8.06 (d, *J* = 8.4 Hz, 2H), 7.54 (d, *J* = 8.4 Hz, 2H), 7.44 (d, *J* = 8.8 Hz, 1H), 7.37 – 7.30 (m, 2H), 7.25 (dd, *J* = 9.0, 7.0 Hz, 1H), 6.80 (d, *J* = 8.8 Hz, 2H), 4.70 (s, 2H), 1.46 (s, 9H).^{13}C NMR ($CDCl_3$, 100 MHz): δ 178.7, 170.7, 160.2, 158.7, 146.0, 136.1 (2C), 132.9, 131.4, 130.9 (2C), 128.5 (2C), 128.2 (2C), 128.0, 127.4, 126.7 (2C), 115.2 (2C), 109.1, 59.7, 34.7, 29.0 (3C). HR MS-ESI: for $C_{27}H_{23}Cl_2NO_4$ calculated 497.9065, found *m/z* 496.1501 [M - H]$^-$.

4'-((3-(2-bromo-6-chlorophenyl)-5-(tert-butyl)isoxazol-4-yl)methoxy)-[1,1'-biphenyl]-4-carboxylic acid (4e). The hydrolysis crude was purified by preparative HPLC employing an Agilent Pre-C18 column (30x100 mm, 5 μm) with solvent A (water 0.1% TFA) and B (ACN 0.1% TFA) in a linear gradient from 60% B to 95% B in 15 min to afford compound **4e** (R_t = 12.5 min, 62% yield). ^{1}H NMR (400 MHz, $CDCl_3$) δ 8.06 (d, *J* = 8.3 Hz, 2H), 7.57 (dd, *J* = 8.3, 1.1 Hz, 3H), 7.50 (d, *J* = 8.8 Hz, 2H), 7.43 (dd, *J* = 8.1, 1.1 Hz, 1H), 7.22 (t, *J* = 8.1 Hz, 1H), 6.86 (d, *J* = 8.8 Hz, 2H), 4.76 (d, *J* = 2.6 Hz, 2H), 1.53 (s, 9H). ^{13}C NMR ($CDCl_3$, 100 MHz): δ 178.7, 171.5, 161.8, 158.7, 146.0, 135.9, 132.9, 131.7, 131.4, 130.9 (2C), 129.9, 128.8, 128.5 (2C), 127.6, 126.7 (2C), 125.4, 115.2 (2C), 108.9, 59.7, 34.7, 29.0 (3C). HR MS-ESI: for $C_{27}H_{23}BrClNO_4$ calculated 539.0499, found *m/z* 538.0365 $[M - H]^-$.

4-((4-((5-(tert-butyl)-3-(2,6-dichlorophenyl)isoxazol-4-yl)methoxy)benzyl)oxy)benzoic acid (4f). The hydrolysis crude was purified through flash column chromatography on silica gel (MeOH 3% in DCM) to afford compound **4f** (52% yield). ^{1}H NMR (DMSO-d6, 400 MHz): δ 12.6 (1H, br s, COO**H**), 7.86 (d, *J* = 8.8 Hz, 2H), 7.87 (d, *J* = 8.4 Hz, 2H), 7.61 (dd, *J* = 8.1, 1.1 Hz, 2H), 7.53 (dd, *J* = 8.8, 7.0 Hz, 1H), 7.31 (d, *J* = 8.7 Hz, 2H), 7.05 (d, *J* = 8.9 Hz, 1H), 6.82 (d, *J* = 8.7 Hz, 2H), 5.05 (s, 2H), 4.77 (s, 2H), 1.45 (s, 9H). ^{13}C NMR (DMSO-d6, 100 MHz): δ 177.7, 166.9, 161.9, 159.7, 157.6, 134.7 (2C), 132.4 (2C), 131.2 (2C), 129.5 (2C), 129.0, 128.4 (2C), 127.1, 114.5 (2C), 114.4 (2C), 109.1, 69.1, 59.2, 34.0, 28.4 (3C). HR MS-ESI: for $C_{28}H_{26}ClNO_5$ calculated 491.1500, found *m/z* 492.1573 $[M + H]^+$.

3-((4-((5-(tert-butyl)-3-(2,6-dichlorophenyl)isoxazol-4-yl)methoxy)benzyl)oxy)benzoic acid (4g). The hydrolysis crude was purified through flash column chromatography on silica gel (MeOH 8% in DCM) to afford compound **4g** (38% yield). ^{1}H NMR ($CDCl_3$, 400 MHz): δ 7.73 – 7.64 (m, 2H), 7.43 – 7.25 (m, 7H), 7.18 (d, *J* = 8.1 Hz, 1H), 6.78 (d, *J* = 8.6 Hz 2H), 5.00 (s, 2H), 4.72 (s, 2H), 1.51 (s, 9H). ^{13}C NMR ($CDCl_3$, 100 MHz): δ 178.6, 160.2, 158.9, 158.3 136.1 (2C), 131.3 (2C), 129.7

(2C), 129.45 (2C), 129.1, 128.2 (2C), 128.0, 123.0, 121.2, 115.5, 114.9 (2C), 109.1, 70.0, 59.6, 34.6, 28.9 (3C). HR MS-ESI: for $C_{28}H_{26}ClNO_5$ calculated 491.1500, found *m/z* 492.1470 $[M + H]^+$.

4-((4-((3-(2-bromo-6-chlorophenyl)-5-(tert-butyl)isoxazol-4-yl)methoxy)benzyl)oxy)benzoic acid (4h). The hydrolysis crude was purified through flash column chromatography on silica gel (MeOH 1% in DCM) to afford compound **4h** (59% yield). ^{1}H NMR (DMSO-d6, 400 MHz): δ 12.60 (1H, br s, COO**H**), 7.87 (d, *J* = 8.8 Hz, 2H), 7.75 (dd, *J* = 8.1, 1.1 Hz, 1H), 7.64 (dd, *J* = 8.1, 1.1 Hz, 1H), 7.44 (t, *J* = 8.1 Hz, 1H), 7.31 (d, *J* = 8.7 Hz, 2H), 7.05 (d, *J* = 9.0 Hz, 1H), 6.82 (d, *J* = 8.7 Hz, 1H), 5.06 (d, *J* = 4.0 Hz, 2H), 4.86 – 4.61 (m, 2H), 1.45 (s, 9H). ^{13}C NMR (DMSO-d6, 100 MHz): δ 177.6, 166.9, 161.9, 161.3, 157.7, 134.5, 132.7, 131.5, 131.2 (2C), 129.5 (2C), 128.9 (2C), 128.8, 124.5, 123.0, 114.5 (2C), 114.4 (2C), 108.9, 69.1, 59.2, 34.0, 28.4 (3C). HR MS-ESI: for $C_{28}H_{25}BrClNO_5$ calculated 569.0605, found *m/z* 570.0701 $[M + H]^+$.

3-((4-((3-(2-bromo-6-chlorophenyl)-5-(tert-butyl)isoxazol-4-yl)methoxy)benzyl)oxy)benzoic acid (4i). The hydrolysis crude was purified through flash column chromatography on silica gel (MeOH 2% in DCM) to afford compound **4i** (48% yield). ^{1}H NMR ($CDCl_3$, 400 MHz): δ 7.74 – 7.64 (m, 2H), 7.56 (dd, *J* = 8.1, 1.1 Hz, 1H), 7.42 (dd, *J* = 8.1, 1.1 Hz, 1H), 7.37 (t, *J* = 8.0 Hz, 1H), 7.31 (d, *J* = 8.6 Hz, 2H), 7.22 (t, *J* = 8.1 Hz, 1H), 7.20 – 7.12 (m, 1H), 6.80 (d, *J* = 8.6 Hz, 2H), 5.01 (s, 2H), 4.72 (d, *J* = 2.7 Hz, 2H), 1.51 (s, 9H). ^{13}C NMR ($CDCl_3$, 100 MHz): δ 178.7, 169.6, 161.8, 158.9, 158.4, 135.9, 131.6, 131.3, 130.4, 129.9, 129.7, 129.4 (2C), 129.1, 128.7, 125.3, 122.9, 121.2, 115.5, 114.9 (2C), 108.9, 70.0, 59.6, 34.7, 29.0 (3C). HR MS-ESI: for $C_{28}H_{25}BrClNO_5$ calculated 569.0605, found *m/z* 570.0652 $[M + H]^+$.

AlphaScreen on FXR-SRC1

The ability to mediate the cofactor recruitment was evaluated by employing AlphaScreen GST Detection Kit (Revvity). Particularly, FXR agonism was evaluated employing 10 nM FXR-LBD GST-fused (Thermo Scientific) and 30 nM of biotinylated SRC1 peptide (CPSSHSSLTERHKILHRLLQEGSPS) in the presence of 20 μg/mL donor and acceptor beads in a

buffer containing 50 mM Tris-HCl (pH 7.4), 20 mM KCl, 1 mM DTT, and 0.1% BSA. Incubations were performed in a final volume of 25 µL, employing a 384 wells Optiplate. Alpha signal was measured with Envision 2105 (Perkin Elmer) multi-mode plate reader. Compounds were tested at concentrations ranging from 0.1 nM to 80 µM for potency evaluation and the 5 µM concentration point was used to assess the efficacy.

AlphaScreen on LIF-LIFR

Recombinant human LIFR (His-Tag) and LIF (biotinylated) were purchased from Sino Biologicals (Sino Biological Europe GmbH, Dusseldorf, Germany) and R&D Systems (Abingdon, UK), respectively, and both were reconstituted as required by the manufacturer. Inhibition of LIFR/LIF binding was measured by AlphaScreen, in white, low-volume, 384-well AlphaPlates (PerkinElmer, Waltham, MA, USA) using a final volume of 15 µL and an assay buffer containing 25 mM Hepes (pH 7.4), 100 mM NaCl, and 0.005% Kathon. The concentration of DMSO in each well was maintained at 5% v/v. LIFR (His-Tag, final concentration 4.5 nM) was incubated with the compounds or DMSO for 45 min under continuous shaking. Then, LIF was added (biotinylated, final concentration 9 nM), and the samples were incubated for 15 min prior to adding nickel chelate acceptor beads (final concentration 20 ng/µL) for 30 min. Then, streptavidin donor beads were added (final concentration 20 ng/µL), and the plate was incubated in the dark for 2 h and then read in an EnSpire Alpha multimode plate reader (PerkinElmer, Waltham, MA, USA).

Solubility and LogD Measurements

10 µL of a 10 mM solution of each compound were diluted either in 490 µL of PBS pH 7.4 or MeOH and shaken at 250 rpm for 24 h at rt. Tubes were subsequently centrifuged for 15 min at 15,000 rpm and supernatants filtered using 0.22 mm cartridges. 10 µL of each sample were further diluted in 490 µL of MeOH and analyzed by LC-MS, using a Kinetex® 2.6 µ Biphenyl 100 Å, 100x2.1 mm LC column. Water (0,1% Formic Acid) was employed as Solvent A and acetonitrile (0,1% Formic Acid) as Solvent B. The gradient used was as follows: 0.00 min 45% B, 2.50 min 45% B, 6.00 min 95% B,

10.00 min 95% B, 10.10 min 45% B and 13.00 min 45% B. The ratio of mass signal area obtained in PBS and in organic solvent was then calculated and used to determine solubility of each compound. For LogD measurement, 40 µL of each compound (10 mM) were diluted in 1960 µL of PBS pH 7.4/Octanol (1:1) and the mixtures were shaken for 2 h at rt. Then, organic and aqueous phases were separated, and after proper dilution, each phase was analyzed by LC-MS. LogD was calculated as the logarithm of the ratio of compounds concentrations in octanol and PBS.

***In vitro* Metabolic Stability**

Human liver S9 fraction (Sigma-Aldrich, St. Louis, MO, USA) was used. All incubations were performed in duplicate in a thermoblock (Dlab dry bath HB 120-S) at 37 °C. Each incubation mixture contained the compound at 1 µM final concentration with 0.5% DMSO, Human liver S9 fraction (0.3 mg of protein per mL), 5 mM taurine, 5 mM glycine, 5 mM glucose 6-phosphate, 5 mM GSH, 1 mM NADPH, 1 mM ATP, 0.4 mM CoA, 0.4 mM UDPGA, 0.1 mM PAPS, and 0.4 $U \cdot mL^{-1}$ glucose 6-phosphate dehydrogenase, in a total volume of 0.25 mL. The incubation buffer was 50 mM potassium phosphate buffer (pH 7.4), containing 5 mM $MgCl_2$. At defined times of 0, 5, 15, 30, 45, 60, and 90 min after S9 addition, 25 µL aliquots were withdrawn and the enzymatic reaction was quenched with 100 µL of ice-cold ACN. The samples were centrifuged for 10 min at 10,000 rpm, and the supernatants were transferred into vials for LC-MS analysis, employing the conditions described above. The slope of the linear regression of the curve obtained by reporting the natural logarithm of compound area versus incubation time (−k) was used in the conversion to *in vitro* $t_{1/2}$ values, calculated as $t_{1/2} = -\ln(2)/k$. *In vitro* intrinsic clearance (Cl_{int} expressed as µL/min/mg) was obtained by first calculating V using the formula: V = volume of reaction (µL)/protein of liver microsomes (mg); intrinsic clearance was then calculated as: $Cl_{int} = (V \times \ln 2)/t_{1/2}$. Testosterone was used as positive control for phase I enzymes, and 7-hydroxycoumarin was used as positive control for phase II enzymes.

Parallel Artificial Membrane Permeation Assays (PAMPA)

The assay was prepared as follows: 300 µL of PBS pH 7.4 (5% DMSO) were placed in the acceptor wells. A phosphatidylcholine (PC) solution was obtained by dissolving and vortexing PC at 1% w/v in dodecane and solubilized using an ultrasound bath until a clear solution was obtained. 5 mL of this solution was deposited on the membrane portion of the donor well. 150 µL of each molecule, at 100 µM final concentration (5% DMSO), were pipetted in the acceptor wells. The acceptor (Multiscreen transport Receiver Plate, 96 well, polystyrene, Millipore) and donor plates (Multiscreen Filter Plates, IP, 0.45 mm, clear, Hydrophobic PVDF, Millipore) were subsequently assembled and incubated for 5 h under gentle orbital shaking. The experiment was conducted in duplicate. Lucifer yellow was used as a negative control to establish the integrity of the membrane, quantifying its concentration in both acceptor and donor solutions using fluorescence. Verapamil was used as a positive, high permeable, standard. Acceptor, donor and equilibrium solutions, along with the original 100 µM stock solutions, were analyzed by LC-MS, using the same conditions described above.

Effective permeability was calculated using the following formula: $P_e = Log[C \times -ln\left(1 - \frac{AUC\ Acc}{AUC\ eq}\right)]$

where C is calculated as: $C = \frac{Vdon \times Vacc}{(Vdon + Vacc) \times Area \times Time(s)}$

The equilibrium condition (eq) is defined as the concentration of the molecule as if the acceptor and donor compartments were combined, and it was prepared diluting the original stock solution to a final concentration of 33.3 mM.

2D Colture Cell Lines

Hepatic cancer cells line (HepG2). Cells were from ATCC (Manassas, VA; USA). The cells were grown in MEM (Sigma-Merck Life Science S.r.l. Milan, Italy) medium supplemented with 10% Fetal Bovine Serum (FBS), 1% L-Glutamine, 1% Penicillin/Streptomycin.

Human hepatic stellate cells (HSC). HSC cells were provided by Innoprot (REF: P10653) and they were grown in their specific stellate cell medium (SteCM) enriched with fetal bovine serum, stellate cell growth supplement (SteCGS) and Penicillin/Streptomycin solution (Innoprot, REF: P60126).

Murine macrophage cells (RAW), from ATCC (Manassas, VA; USA). The cells were grown in d-MEM (Sigma-Merck Life Science S.r.l. Milan, Italy) medium supplemented with 10% Fetal Bovine Serum (FBS), 1% L-Glutamine, 1% Penicillin/Streptomycin.

All cultures were maintained in a humidified 5% CO_2 atmosphere, 37 °C. The cells were free from Mycoplasma contamination, as confirmed using Mycoplasma PCR Detection (Sigma).

Transactivation assay

To evaluate the FXR/RXR signaling, HepG2 cells were transiently transfected with 200 ng of the reporter vector containing the response element p(hsp27) -TK-LUC, 100 ng of pSG5-FXR, 100 ng of pSG5-RXR, and 100 of pGL4.70 (Promega, Madison WI), a vector encoding the human Renilla gene. The next day, the cells were stimulated with 10 μM CDCA and compound **3a** or compound **4d** at 0.01, 0.1, 1, 5, and 10 μM, to get a dose-response curve. HepG2 cells were also transfected with 200 ng of the reporter vector containing the response element Pgl4.47, 100 ng of LIFR, 100 ng of IL6ST(gp130), and 100 of pGL4.70 (Promega, Madison WI), a vector encoding the human Renilla gene. The next day, the cells were stimulated with 10 ng/mL LIF and compound **3a** or compound **4d** at 1, 10, 20, and 50 μM, to get a dose-response curve. After treatments, the cells were lysed in 100 μL of lysis buffer (25 mM Tris-phosphate, pH 7.8; 2 mM dithiothreitol (DTT); 10% glycerol; 1% Triton X-100), and 10 μL of cellular lysate was assayed for luciferase activity using the luciferase assay system and normalized with Renilla activities (Biotium). Luminescence was measured using Glomax 20/20 luminometer (Promega). Luciferase activities were assayed and normalized with Renilla activities.

RNA extraction

RAW cells were first seeded on a 6 well plate (2 mL/well) and then exposed to LPS (50 nM) alone or in combination with compound **3a** and compound **4d** (10 μM) for 24 h.

HSC (2,5× 105 cells per well) were seeded on a 6 well plate (2 mL/well) and then exposed to LIF (200 nM) alone or in combination with compound **3a** and compound **4d** (10 and 50 μM) for 24 h.

HepG2 (2,5× 10^5 cells per well) were seeded on a 6 well plate (2 mL/well) and then exposed to compound **3a** and compound **4d** (10 μM) for 24 h. The next day RNA was extracted from the cultures to evaluate mRNA gene expression. Total mRNA extraction from cells and tissue samples and cells was performed using Tri-Reagent (Zymo Research) and Direct-zol™ RNA MiniPrep w/ Zymo-Spin™ IIC Columns (Zymo Research, Irvine, CA). After purification from genomic DNA using DNase I (Thermo Fisher Scientific, Waltham, MA). RNA extracted was used for gene expression analysis via RNA-seq or qPCR analysis.

Reverse and Real Time (RT) PCR

After purification from genomic DNA using DNase I (Thermo Fisher Scientific, Waltham, MA), 1-2 μg of RNA from each sample was reverse transcribed using Kit FastGene Scriptase Basic (Nippon Genetics, Mariaweilerstraße, Düren, Germaniain) in 20 μL of reaction volume; 50 ng of cDNA was amplified in a 20 μL solution containing 200 nM each primer and 10 μL of PowerUp™ SYBR™ Green Master Mix (Thermo Fisher Scientific, Waltham, MA). All reactions were performed in triplicate using the following thermal cycling conditions: 2 min at 95 °C, followed by 40 cycles of 95 °C for 3 s, 60 °C for 30 s, using a QuantStudio 3 system (Applied Biosystems, Foster City, CA). The relative mRNA expression was calculated according to the ΔC_t method. Primers were designed using the software PRIMER3 (http://frodo.wi.mit.edu/primer3/) using published data obtained from the NCBI database The primers used for mouse genes were as follows [forward (for) and reverse (rev)]: Shp (Homo Sapiens; for GAATATGCCTGCCTGAAAGG; rev TCCAGGACTTCACACAGCAC), Cyp7a1 (Homo sapiens; for GACACACCTCGTGGTCCTCT; rev TTTCATTGCTTCTGGGTTCC), Ostα (Homo sapiens; for TGTTGGGCCCTTTCCAATAC; rev GGCTCCCATGTTCTGCTCAC), Ostβ (Homo sapiens;

for CAGGCAAGCAGAAAAGAAAAG; rev CCGGAAGGAAAACTGACA), Ccl2 (Mus musculus; for AAGAGGATCACCAGCAGCAG; rev TCTGGACCCATTCCTTCTTG), Cxcl2 (Mus musculus; for TCCAGAGCTTGAGTGTGACG; rev GCTTCAGGGTCAAGGCAAAC), Il-6 (Mus musculus; for CTTCACAAGTCGGAGGCTTA; rev TTCTGCAAGTGCATCATCGT), Col1a1 (Homo sapiens; for CCCAAGGCTTCCAAGGTC; rev GACCAGGTTTTCCAGCTTCC), αSma (Homo sapiens; for GTGTTCCCGTCCATCGTG; rev CTCTTGCTCTGAGCCTCGTC), Col1a1 (Mus musculus; for TGACTGGAAGAGCGGAGAGT; rev AGACGGCTGAGTAGGGAACA), αSma (Mus musculus; for AGAGCTACGAACTGCCTGAC; rev TAGGTGGTTTCGTGGATGCC), Lif (Mus musculus; for GAATCAACTGGCACAGCTCA; rev GTTAGGCGCACATAGCTTTT), Lifr (Mus musculus; for CTGGTGATCACGAAGTCACA; rev GATCTCGGGAGTCTCTGGA), Fxr (Mus musculus; for AGCTTCCAGGGTTTCAGACA; rev CTTCCAACAGGTCTGCATGA), Shp (Mus musculus; for ACGATCCTCTTCAACCCAGA; rev AGGGCTCCAAGACTTCACAC), Cyp7a1 (Mus musculus; for AGGCATTTGGACACAGAAGC; rev TGCATCATGGCTTCAGAGAG), Ostβ (Mus musculus; for GGAACTGCTGGAAGAAATGC; rev CAGGAGGAACATGCTTGTCA), Bsep (Mus musculus; for GATGCTTCCCAAGTTCAAGG; rev TAAAGAGGAAGGCGATGAGC).

Animals and fibrosis protocols

C57BL/6J male mice, purchased from Charles River, were maintained in the animal facility of the University of Perugia. Mice were housed under controlled temperatures conditions (22 °C) and photoperiods (12:12-hour light/dark cycle), with unrestricted access to standard mouse chow and tap water. They were acclimated to these conditions for at least 7 d prior to inclusion in any experiment. The study complied in agreement with the EU/Italian law and received approval from the Ethical Committee of the University of Perugia and the National Committee of the Italian Ministry of Health (permit no. 214/2017-PR). Animal health and body conditions were monitored daily by the facility veterinarian. Only male mice aged 10-12 weeks were used in each experiment, 5-8 mice per group.

Liver fibrosis was induced by intraperitoneal (i.p.) injection of carbon tetrachloride (CCl_4) at the dose of 500 μL/Kg, dissolved in an equal volume of olive oil, administered twice a week for one week as previously described.[58] CCl_4-mice were randomized to receive compound **3a** at the doses of 3, 10 and 30 mg/Kg/day by gavage from the first day of the experiment. Mice were sacrificed one week later. At the end of the experiment, mice were euthanized with overdose of anesthetic and blood and liver were collected for biochemical, histological and gene expression analyses.

Computational studies

Molecular docking calculations and MD simulations were conducted to elucidate the binding mode of **3a** within both FXR and LIFR binding pockets.

Receptor and ligand preparation

The crystal structure of the homo sapiens FXR in the active conformation (PDB ID 3DCT)[51] and the human LIFR, *h*LIFR (PDB ID: 3E0G)[59] were downloaded from the Protein Data Bank website (www.rcsb.org). The nuclear receptor coactivator 1, the FXR co-crystallized ligand GW4064, and water molecules were removed. Both the receptors were prepared using the Protein Preparation Wizard tool implemented in Maestro GUI ver. 11.8 [60] to assign bond orders, add hydrogen atoms, adjust disulfide bonds, add caps to chains break, and assign residues protonation state at pH 7.4. The tridimensional structure of compound **3a** was generated using the graphical user interface (GUI) of Maestro ver. 11.8.[60] The protonation state at pH 7.4 in water was calculated using the Epik module.[61] Finally, the ligand was minimized using the OPLS2005 [62] force field through 2500 iteration steps of the Polak-Ribiere Conjugate Gradient (PRCG)[63] algorithm.

Docking calculations

Docking calculations on FXR were carried out with the Glide software package,[64] using the standard precision (SP) algorithm of the GlideScore function and the OPLS 2005 [62] force field and a grid box of 23 × 23 × 23 Å centered in the ligand orthosteric binding pocket. A total of 100 poses were generated, and the conformational sampling of the ligand was enhanced by 4 times. Docking

conformations of **3a** were then clustered based on its atomic RMSD. Globally, five clusters were obtained and, among them, only the conformation included in the most populated cluster with both the Glide Emodel and GlideScore lowest-energy value was considered. On *h*LIFR receptor, docking calculations were carried out with the QM-Polarized Ligands Docking (QPLD), [65] followed by an Induced Fit Docking procedure.[66] The centroid of the *h*LIFR binding site defined by the L2-L3 loops was used to generate the grid box with the default coordinate dimension (10.0 Å). Ten docking poses were saved during the QPLD step and the best-scored were submitted to the IFD procedure using the extended sampling protocol, by generating 80 poses with an energy window for the ligand conformational sampling of 2.5 kcal/mol.

MD simulations

MDs were performed with the CUDA version of Amber22[67] suite using the Amber ff14SB,[68] and the General Amber Force Field (GAFF2) [69] parameters for the proteins and compound **3a**, respectively. In particular, ligand charges were calculated using the restrained electrostatic potential (RESP) fitting procedure. Firstly, the Gaussian16 package was used to calculate the ligand ESP using the 6-31G* basis set at the Hartree-Fock level of theory. The Antechamber module implemented in the AmberTools23 package allowed to generate ligand topology with the RESP charges coupled with the general amber force field (GAFF2) parameters. Both systems were immersed in a pre-equilibrated octahedral box of 10 Å for both FXR and *h*LIFR of TIP3P water molecules and then, neutralized. Subsequently, each system underwent a multi-step minimization process with an energy gradient convergence criterion set to 0.01 kcal/mol Å ^{2}. This process involved: (i) 5000 minimization steps (2500 using the steepest descent method and 2500 using the conjugate gradient method) involving only hydrogen atoms; (ii) 20,000 minimization steps (10,000 using the steepest descent method and 10,000 using the conjugate gradient method) involving water and hydrogen atoms, while restraining the solute; (iii) 50,000 minimization steps (25,000 using the steepest descent method and 25,000 using the conjugate gradient method) involving only the side chains of the protein, water, and hydrogen

atoms; (iv) 100,000 minimization steps (50,000 using the steepest descent method and 50,000 using the conjugate gradient method) involving complete minimization. An equilibration protocol of water molecules, ions, and protein side chains occurred in the following steps: (i) 5 ns of NVT equilibration with the Langevin thermostat, gradually heating from 0 to 300 K while scaling down solute restraints from a force constant of 10 to 1 kcal/mol Å; (ii) 5 ns of NPT equilibration at 1 atm with the Berendsen thermostat, gradually scaling down restraints from 1.0 to 0.1 kcal/mol $Å^2$; (iii) 5 ns of NPT equilibration with no restraints. Finally, three independent production runs of 500 ns each were conducted for each system using a timestep of 2 fs. The SHAKE algorithm was employed for bonds containing hydrogen atoms, in conjunction with periodic boundary conditions at constant pressure and temperature. Long-range electrostatic interactions were treated using the particle mesh Ewald (PME)[70] method with a cutoff of 10 Å for nonbonded interactions.

MD trajectories were visualized using VMD software, [71] while clustering and analysis procedures were performed through the CPPTRAJ module. For the most representative cluster population, intermolecular interaction energies were analyzed via the Molecular Mechanics/Generalized Born Surface Area (MM/ GBSA) equation, using the MMPBSA.py script of the AMBER22 package.

MD simulations were carried out on NVIDIA RTX A6000 and A5000 GPUs. All figures were rendered by UCSF Chimera.[72]

Supporting Information Available. This material is available free of charge via the Internet at http://pubs.acs.org.

^{1}H and ^{13}C NMR of compounds **1d-4i**, HPLC traces of compounds **3a**, **3c**, **3e**, **4b**, and **4d**. *In vitro* agonism and antagonism profiles of selected compounds and transactivation assay data on FXR and LIFR of compounds **1c**, **3a**, **3c**, **3e**, **4b**, and **4d**. Binding mode of **3a** within both FXR and LIFR binding pockets (PDF).

The molecular string of the compounds (CSV)

The atomic coordinates of the molecular complexes discussed are available on the public repository Zenodo https://doi.org/10.5281/zenodo.13712504[73]

Author Contributions

P.R., C.F., V.S., and A.Z. designed and performed synthesis; C.d.G., C.M., G.U., S.M., M.B., M.Bi., and S.F. designed and performed pharmacological experiments; C.C., E.M., L.S., M.C.M. designed and performed AlphaScreen experiments, pharmacokinetics, and LC-MS experiments; B.F., A.L., F.M., and B.C. designed and performed the computational studies, analyzed, and interpreted the data. All the authors contributed to manuscript writing and approved the final version.

Conflict of Interest

The authors declare the following Conflict of Interest: S.F. and A.Z. have filed the Italian patent application no. 102018000007265 and the corresponding PCT (PCT/IB2019/056114).

Acknowledgements. This work was partially supported by grant from the Italian MIUR/PRIN 2022 PNRR (P20227JB3W).

Abbreviations.

CCl_4, carbon tetrachloride; CCR, CC chemokine receptor; CDCA, chenodeoxycholic acid; DIAD, diisopropyl azodicarboxylate; DMF, N,N-dimethylformamide; ECM, extracellular matrix; FXR, farnesoid X receptor; GC, gastric adenocarcinoma; GLP-1, Glucagon-like peptide-1; GPBAR1, G protein-coupled bile acid receptor; HSCs, hepatic stellate cells; IBDs, inflammatory bowel diseases; IFD, Induced Fit Docking; IL-6, interleukin 6; LBD, ligand binding domain; $LiBH_4$, lithium borohydride; LIF, leukaemia inhibitory factor; LIFR, leukaemia inhibitory factor receptor; MAFLD, Metabolic dysfunction–associated fatty liver disease; MASH, metabolic dysfunction-associated steatohepatitis; MASLD, metabolic dysfunction-associated liver disease; IFD, Induced-Fit Docking; MDs, molecular dynamics; MM/GBSA, molecular mechanics/generalized born surface area; MM/PBSA, molecular mechanics Poisson-Boltzmann surface area; PDAC, pancreatic ductal adenocarcinoma; PDGF, platelet-derived growth factor; PDGF-β, platelet derived growth factor-β;

PK, pharmacokinetics; PPARs, peroxisome proliferator activated receptors; PPh_3, triphenylphosphine; α-SMA, alpha Smooth Muscle Actin; TGFβ, Transforming growth factor β; THF, tetrahydrofuran; VEGF, vascular endothelial growth factor; VEGFR vascular endothelial growth factor receptor

References

(1) Tacke, F.; Puengel, T.; Loomba, R.; Friedman, S. L. An Integrated View of Anti-Inflammatory and Antifibrotic Targets for the Treatment of NASH. *J. Hepatol.* **2023**, *79* (2), 552-566. https://doi.org/10.1016/j.jhep.2023.03.038.

(2) Friedman, S. L.; Pinzani, M. Hepatic Fibrosis 2022: Unmet Needs and a Blueprint for the Future. *Hepatology* **2022**, *75* (2), 473-488. https://doi.org/10.1002/hep.32285.

(3) Lefebvre, E.; Moyle, G.; Reshef, R.; Richman, L. P.; Thompson, M.; Hong, F.; Chou, H. L.; Hashiguchi, T.; Plato, C.; Poulin, D.; Richards, T.; Yoneyama, H.; Jenkins, H.; Wolfgang, G.; Friedman, S. L. Antifibrotic Effects of the Dual CCR2/CCR5 Antagonist Cenicriviroc in Animal Models of Liver and Kidney Fibrosis. *PLoS One* **2016**, *11* (6), e0158156. https://doi.org/10.1371/journal.pone.0158156.

(4) Horn, P.; Tacke, F. Metabolic Reprogramming in Liver Fibrosis. *Cell Metab.* **2024**, *36* (7), 1439-1455. https://doi.org/10.1016/j.cmet.2024.05.003.

(5) Lee, Y. A.; Friedman, S. L. Inflammatory and Fibrotic Mechanisms in NAFLD-Implications for New Treatment Strategies. *J. Intern. Med.* **2021**, *291* (1), 11-31. https://doi.org/10.1111/joim.13380.

(6) Higashi, T.; Friedman, S. L.; Hoshida, Y. Hepatic Stellate Cells as Key Target in Liver Fibrosis. *Adv. Drug Deliv. Rev.* **2017**, *121*, 27-42. https://doi.org/10.1016/j.addr.2017.05.007.

(7) Trivedi, P.; Wang, S.; Friedman, S. L. The Power of Plasticity-Metabolic Regulation of

Hepatic Stellate Cells. *Cell Metab* **2021**, *33* (2), 242–257. https://doi.org/10.1016/j.cmet.2020.10.026.

(8) Karin, M.; Kim, J. Y. MASH as an Emerging Cause of Hepatocellular Carcinoma: Current Knowledge and Future Perspectives. *Mol. Oncol.* **2024**. https://doi.org/10.1002/1878-0261.13685.

(9) Tsuchida, T.; Friedman, S. L. Mechanisms of Hepatic Stellate Cell Activation. *Nat Rev Gastroenterol Hepatol* **2017**, *14* (7), 397-411. https://doi.org/10.1038/nrgastro.2017.38.

(10) Ratziu, V.; Sanyal, A.; Harrison, S. A.; Wong, V. W.-S.; Francque, S.; Goodman, Z.; Aithal, G. P.; Kowdley, K. V; Seyedkazemi, S.; Fischer, L.; Loomba, R.; Abdelmalek, M. F.; Tacke, F. Cenicriviroc Treatment for Adults With Nonalcoholic Steatohepatitis and Fibrosis: Final Analysis of the Phase 2b CENTAUR Study. *Hepatology* **2020**, *72* (3), 892-905. https://doi.org/10.1002/hep.31108.

(11) Ratziu, V.; Friedman, S. L. Why Do So Many Nonalcoholic Steatohepatitis Trials Fail? *Gastroenterology* **2023**, *165* (1), 5-10. https://doi.org/10.1053/j.gastro.2020.05.046.

(12) Rinella, M. E.; Lazarus, J. V; Ratziu, V.; Francque, S. M.; Sanyal, A. J.; Kanwal, F.; Romero, D.; Abdelmalek, M. F.; Anstee, Q. M.; Arab, J. P.; Arrese, M.; Bataller, R.; Beuers, U.; Boursier, J.; Bugianesi, E.; Byrne, C.; Castro Narro, G. E.; Chowdhury, A.; Cortez-Pinto, H.; Cryer, D.; Cusi, K.; El-Kassas, M.; Klein, S.; Eskridge, W.; Fan, J.; Gawrieh, S.; Guy, C. D.; Harrison, S. A.; Kim, S. U.; Koot, B.; Korenjak, M.; Kowdley, K.; Lacaille, F.; Loomba, R.; Mitchell-Thain, R.; Morgan, T. R.; Powell, E.; Roden, M.; Romero-Gómez, M.; Silva, M.; Singh, S. P.; Sookoian, S. C.; Spearman, C. W.; Tiniakos, D.; Valenti, L.; Vos, M. B.; Wong, V. W.-S.; Xanthakos, S.; Yilmaz, Y.; Younossi, Z.; Hobbs, A.; Villota-Rivas, M.; Newsome, P. N. A Multi-Society Delphi Consensus Statement on New Fatty Liver Disease Nomenclature. *Hepatology* **2023**. https://doi.org/10.1097/HEP.0000000000000520.

(13) Ratziu, V.; Harrison, S. A.; Francque, S.; Bedossa, P.; Lehert, P.; Serfaty, L.; Romero-Gomez,

M.; Boursier, J.; Abdelmalek, M.; Caldwell, S.; Drenth, J.; Anstee, Q. M.; Hum, D.; Hanf, R.; Roudot, A.; Megnien, S.; Staels, B.; Sanyal, A. Elafibranor, an Agonist of the Peroxisome Proliferator-Activated Receptor-α and -δ, Induces Resolution of Nonalcoholic Steatohepatitis Without Fibrosis Worsening. *Gastroenterology* **2016**, *150* (5), 1147-1159.e5. https://doi.org/10.1053/j.gastro.2016.01.038.

(14) Younossi, Z. M.; Ratziu, V.; Loomba, R.; Rinella, M.; Anstee, Q. M.; Goodman, Z.; Bedossa, P.; Geier, A.; Beckebaum, S.; Newsome, P. N.; Sheridan, D.; Sheikh, M. Y.; Trotter, J.; Knapple, W.; Lawitz, E.; Abdelmalek, M. F.; Kowdley, K. V; Montano-Loza, A. J.; Boursier, J.; Mathurin, P.; Bugianesi, E.; Mazzella, G.; Olveira, A.; Cortez-Pinto, H.; Graupera, I.; Orr, D.; Gluud, L. L.; Dufour, J. F.; Shapiro, D.; Campagna, J.; Zaru, L.; MacConell, L.; Shringarpure, R.; Harrison, S.; Sanyal, A. J.; Investigators, R. S. Obeticholic Acid for the Treatment of Non-Alcoholic Steatohepatitis: Interim Analysis from a Multicentre, Randomised, Placebo-Controlled Phase 3 Trial. *Lancet* **2019**, *394* (10215), 2184-2196. https://doi.org/10.1016/S0140-6736(19)33041-7.

(15) Pellicciari, R.; Fiorucci, S.; Camaioni, E.; Clerici, C.; Costantino, G.; Maloney, P. R. R.; Morelli, A.; Parks, D. J. J.; Willson, T. M. M. 6alpha-Ethyl-Chenodeoxycholic Acid (6-ECDCA), a Potent and Selective FXR Agonist Endowed with Anticholestatic Activity. *J Med Chem* **2002**, *45* (17), 3569-3572. https://doi.org/10.1021/jm025529g.

(16) Patel, K.; Harrison, S. A.; Elkhashab, M.; Trotter, J. F.; Herring, R.; Rojter, S. E.; Kayali, Z.; Wong, V. W.; Greenbloom, S.; Jayakumar, S.; Shiffman, M. L.; Freilich, B.; Lawitz, E. J.; Gane, E. J.; Harting, E.; Xu, J.; Billin, A. N.; Chung, C.; Djedjos, C. S.; Subramanian, G. M.; Myers, R. P.; Middleton, M. S.; Rinella, M.; Noureddin, M. Cilofexor, a Nonsteroidal FXR Agonist, in Patients With Noncirrhotic NASH: A Phase 2 Randomized Controlled Trial. *Hepatology* **2020**, *72* (1), 58-71. https://doi.org/10.1002/hep.31205.

(17) Harrison, S. A.; Bedossa, P.; Guy, C. D.; Schattenberg, J. M.; Loomba, R.; Taub, R.; Labriola,

D.; Moussa, S. E.; Neff, G. W.; Rinella, M. E.; Anstee, Q. M.; Abdelmalek, M. F.; Younossi, Z.; Baum, S. J.; Francque, S.; Charlton, M. R.; Newsome, P. N.; Lanthier, N.; Schiefke, I.; Mangia, A.; Pericàs, J. M.; Patil, R.; Sanyal, A. J.; Noureddin, M.; Bansal, M. B.; Alkhouri, N.; Castera, L.; Rudraraju, M.; Ratziu, V. A Phase 3, Randomized, Controlled Trial of Resmetirom in NASH with Liver Fibrosis. *N. Engl. J. Med.* **2024**, *390* (6), 497-509. https://doi.org/10.1056/NEJMoa2309000.

(18) Nogueiras, R.; Nauck, M. A.; Tschöp, M. H. Gut Hormone Co-Agonists for the Treatment of Obesity: From Bench to Bedside. *Nat. Metab.* **2023**, *5* (6), 933-944. https://doi.org/10.1038/s42255-023-00812-z.

(19) Zhang, C.-Y.; Liu, S.; Yang, M. Treatment of Liver Fibrosis: Past, Current, and Future. *World J. Hepatol.* **2023**, *15* (6), 755-774. https://doi.org/10.4254/wjh.v15.i6.755.

(20) Ratziu, V. A Critical Review of Endpoints for Non-Cirrhotic NASH Therapeutic Trials. *J Hepatol* **2018**, *68* (2), 353-361. https://doi.org/10.1016/j.jhep.2017.12.001.

(21) Casertano, M.; Genovese, M.; Piazza, L.; Balestri, F.; Del Corso, A.; Vito, A.; Paoli, P.; Santi, A.; Imperatore, C.; Menna, M. Identifying Human PTP1B Enzyme Inhibitors from Marine Natural Products: Perspectives for Developing of Novel Insulin-Mimetic Drugs. *Pharmaceuticals* **2022**, *15* (3), 325. https://doi.org/10.3390/ph15030325.

(22) Fiorucci, S.; Sepe, V.; Biagioli, M.; Fiorillo, B.; Rapacciuolo, P.; Distrutti, E.; Zampella, A. Development of Bile Acid Activated Receptors Hybrid Molecules for the Treatment of Inflammatory and Metabolic Disorders. *Biochem. Pharmacol.* **2023**, *216*, 115776. https://doi.org/10.1016/j.bcp.2023.115776.

(23) Fiorucci, S.; Distrutti, E.; Carino, A.; Zampella, A.; Biagioli, M. Bile Acids and Their Receptors in Metabolic Disorders. *Prog Lipid Res* **2021**, *82* (December 2020), 101094. https://doi.org/10.1016/j.plipres.2021.101094.

(24) Forman, B. M.; Goode, E.; Chen, J.; Oro, A. E.; Bradley, D. J.; Perlmann, T.; Noonan, D. J.;

Burka, L. T.; McMorris, T.; Lamph, W. W.; Evans, R. M.; Weinberger, C. Identification of a Nuclear Receptor That Is Activated by Farnesol Metabolites. *Cell* **1995**, *81* (5), 687-693. https://doi.org/10.1016/0092-8674(95)90530-8.

(25) Maruyama, T.; Miyamoto, Y.; Nakamura, T. T. T.; Tamai, Y.; Okada, H.; Sugiyama, E.; Itadani, H.; Tanaka, K.; Nakamura, T. T. T.; Itadani, H.; Tanaka, K.; Nakamura, T. T. T.; Itadani, H.; Tanaka, K.; Nakamura, T. T. T.; Itadani, H.; Tanaka, K. Identification of Membrane-Type Receptor for Bile Acids (M-BAR). *Biochem. Biophys. Res. Commun.* **2002**, *298* (5), 714-719. https://doi.org/10.1016/s0006-291x(02)02550-0.

(26) Marchianò, S.; Biagioli, M.; Morretta, E.; Di Giorgio, C.; Roselli, R.; Bordoni, M.; Bellini, R.; Urbani, G.; Massa, C.; Monti, M. C.; Zampella, A.; Distrutti, E.; Fiorucci, S. Combinatorial Therapy with BAR502 and UDCA Resets FXR and GPBAR1 Signaling and Reverses Liver Histopathology in a Model of NASH. *Sci. Rep.* **2023**, *13* (1), 1602. https://doi.org/10.1038/s41598-023-28647-4.

(27) Carino, A.; Cipriani, S.; Marchianò, S.; Biagioli, M.; Santorelli, C.; Donini, A.; Zampella, A.; Monti, M. C. C.; Fiorucci, S. BAR502, a Dual FXR and GPBAR1 Agonist, Promotes Browning of White Adipose Tissue and Reverses Liver Steatosis and Fibrosis. *Sci Rep* **2017**, *7*, 42801. https://doi.org/10.1038/srep42801.

(28) Loomba, R.; Noureddin, M.; Kowdley, K. V; Kohli, A.; Sheikh, A.; Neff, G.; Bhandari, B. R.; Gunn, N.; Caldwell, S. H.; Goodman, Z.; Wapinski, I.; Resnick, M.; Beck, A. H.; Ding, D.; Jia, C.; Chuang, J. C.; Huss, R. S.; Chung, C.; Subramanian, G. M.; Myers, R. P.; Patel, K.; Borg, B. B.; Ghalib, R.; Kabler, H.; Poulos, J.; Younes, Z.; Elkhashab, M.; Hassanein, T.; Iyer, R.; Ruane, P.; Shiffman, M. L.; Strasser, S.; Wong, V. W.; Alkhouri, N. Combination Therapies Including Cilofexor and Firsocostat for Bridging Fibrosis and Cirrhosis Due to NASH. *Hepatology* **2020**. https://doi.org/10.1002/hep.31622.

(29) Cipriani, S.; Carino, A.; Masullo, D.; Zampella, A.; Distrutti, E.; Fiorucci, S. Decoding the

Role of the Nuclear Receptor SHP in Regulating Hepatic Stellate Cells and Liver Fibrogenesis. *Sci Rep* **2017**, *7*, 41055. https://doi.org/10.1038/srep41055.

(30) Fiorucci, S.; Di Giorgio, C.; Distrutti, E. Obeticholic Acid: An Update of Its Pharmacological Activities in Liver Disorders. *Handb Exp Pharmacol* **2019**, *256*, 283-295. https://doi.org/10.1007/164_2019_227.

(31) Di Giorgio, C.; Bellini, R.; Lupia, A.; Massa, C.; Urbani, G.; Bordoni, M.; Marchianò, S.; Rosselli, R.; De Gregorio, R.; Rapacciuolo, P.; Sepe, V.; Morretta, E.; Monti, M. C.; Moraca, F.; Cari, L.; Ullah, K. R. S.; Natalizi, N.; Graziosi, L.; Distrutti, E.; Biagioli, M.; Catalanotti, B.; Donini, A.; Zampella, A.; Fiorucci, S. The Leukemia Inhibitory Factor Regulates Fibroblast Growth Factor Receptor 4 Transcription in Gastric Cancer. *Cell. Oncol. (Dordr).* **2023**, *47* (2), 695-710. https://doi.org/10.1007/s13402-023-00893-8.

(32) Viswanadhapalli, S.; Dileep, K. V.; Zhang, K. Y. J. J.; Nair, H. B.; Vadlamudi, R. K. Targeting LIF/LIFR Signaling in Cancer. *Genes Dis.* **2022**, *9* (4), 973-980. https://doi.org/10.1016/j.gendis.2021.04.003.

(33) Jorgensen, M. M.; de la Puente, P. Leukemia Inhibitory Factor: An Important Cytokine in Pathologies and Cancer. *Biomolecules* **2022**, *12* (2), 217. https://doi.org/10.3390/biom12020217.

(34) Shi, Y.; Gao, W.; Lytle, N. K.; Huang, P.; Yuan, X.; Dann, A. M.; Ridinger-Saison, M.; DelGiorno, K. E.; Antal, C. E.; Liang, G.; Atkins, A. R.; Erikson, G.; Sun, H.; Meisenhelder, J.; Terenziani, E.; Woo, G.; Fang, L.; Santisakultarm, T. P.; Manor, U.; Xu, R.; Becerra, C. R.; Borazanci, E.; Von Hoff, D. D.; Grandgenett, P. M.; Hollingsworth, M. A.; Leblanc, M.; Umetsu, S. E.; Collisson, E. A.; Scadeng, M.; Lowy, A. M.; Donahue, T. R.; Reya, T.; Downes, M.; Evans, R. M.; Wahl, G. M.; Pawson, T.; Tian, R.; Hunter, T. Targeting LIF-Mediated Paracrine Interaction for Pancreatic Cancer Therapy and Monitoring. *Nature* **2019**, *569* (7754), 131–135. https://doi.org/10.1038/s41586-019-1130-6.

(35) Jones, S. A.; Jenkins, B. J. Recent Insights into Targeting the IL-6 Cytokine Family in Inflammatory Diseases and Cancer. *Nat. Rev. Immunol.* **2018**, *18* (12), 773-789. https://doi.org/10.1038/s41577-018-0066-7.

(36) Nicola, N. A.; Babon, J. J. Leukemia Inhibitory Factor (LIF). *Cytokine Growth Factor Rev.* **2015**, *26* (5), 533–544. https://doi.org/10.1016/j.cytogfr.2015.07.001.

(37) Shahini, A.; Shahini, A. Role of Interleukin-6-Mediated Inflammation in the Pathogenesis of Inflammatory Bowel Disease: Focus on the Available Therapeutic Approaches and Gut Microbiome. *J. Cell Commun. Signal.* **2023**, *17* (1), 55–74. https://doi.org/10.1007/s12079-022-00695-x.

(38) Xu, S.; Yang, X.; Chen, Q.; Liu, Z.; Chen, Y.; Yao, X.; Xiao, A.; Tian, J.; Xie, L.; Zhou, M.; Hu, Z.; Zhu, F.; Xu, X.; Hou, F.; Nie, J. Leukemia Inhibitory Factor Is a Therapeutic Target for Renal Interstitial Fibrosis. *eBioMedicine* **2022**, *86*, 104312. https://doi.org/10.1016/j.ebiom.2022.104312.

(39) Zhou, J.; Jiang, H.; Jiang, H.; Fan, Y.; Zhang, J.; Ma, X.; Yang, X.; Sun, Y.; Zhao, X. The ILEI/LIFR Complex Induces EMT via the Akt and ERK Pathways in Renal Interstitial Fibrosis. *J. Transl. Med.* **2022**, *20* (1), 54. https://doi.org/10.1186/s12967-022-03265-2.

(40) Viswanadhapalli, S.; Luo, Y.; Sareddy, G. R.; Santhamma, B.; Zhou, M.; Li, M.; Ma, S.; Sonavane, R.; Pratap, U. P.; Altwegg, K. A.; Li, X.; Chang, A.; Chávez-Riveros, A.; Dileep, K. V; Zhang, K. Y. J.; Pan, X.; Murali, R.; Bajda, M.; Raj, G. V; Brenner, A. J.; Manthati, V.; Rao, M. K.; Tekmal, R. R.; Nair, H. B.; Nickisch, K. J.; Vadlamudi, R. K. EC359: A First-in-Class Small-Molecule Inhibitor for Targeting Oncogenic LIFR Signaling in Triple-Negative Breast Cancer. *Mol. Cancer Ther.* **2019**, *18* (8), 1341-1354. https://doi.org/10.1158/1535-7163.MCT-18-1258.

(41) Di Giorgio, C.; Lupia, A.; Marchianò, S.; Bordoni, M.; Bellini, R.; Massa, C.; Urbani, G.; Roselli, R.; Moraca, F.; Sepe, V.; Catalanotti, B.; Morretta, E.; Monti, M. C.; Biagioli, M.;

Distrutti, E.; Zampella, A.; Fiorucci, S. Repositioning Mifepristone as a Leukaemia Inhibitory Factor Receptor Antagonist for the Treatment of Pancreatic Adenocarcinoma. *Cells* **2022**, *11* (21), 3482. https://doi.org/10.3390/cells11213482.

(42) Di Giorgio, C.; Morretta, E.; Lupia, A.; Bellini, R.; Massa, C.; Urbani, G.; Bordoni, M.; Marchianò, S.; Lachi, G.; Rapacciuolo, P.; Finamore, C.; Sepe, V.; Chiara Monti, M.; Moraca, F.; Natalizi, N.; Graziosi, L.; Distrutti, E.; Biagioli, M.; Catalanotti, B.; Donini, A.; Zampella, A.; Fiorucci, S. Bile Acids Serve as Endogenous Antagonists of the Leukemia Inhibitory Factor (LIF) Receptor in Oncogenesis. *Biochem. Pharmacol.* **2024**, *223*, 116134. https://doi.org/10.1016/j.bcp.2024.116134.

(43) Di Giorgio, C.; Bellini, R.; Lupia, A.; Massa, C.; Bordoni, M.; Marchianò, S.; Rosselli, R.; Sepe, V.; Rapacciuolo, P.; Moraca, F.; Morretta, E.; Ricci, P.; Urbani, G.; Monti, M. C.; Biagioli, M.; Distrutti, E.; Catalanotti, B.; Zampella, A.; Fiorucci, S. Discovery of BAR502, as Potent Steroidal Antagonist of Leukemia Inhibitory Factor Receptor for the Treatment of Pancreatic Adenocarcinoma. *Front. Oncol.* **2023**, *13*, 1140730. https://doi.org/10.3389/fonc.2023.1140730.

(44) Sepe, V.; Marchianò, S.; Finamore, C.; Baronissi, G.; Di Leva, F. S. S.; Carino, A.; Biagioli, M.; Fiorucci, C.; Cassiano, C.; Monti, M. C. C.; Del Gaudio, F.; Novellino, E.; Limongelli, V.; Fiorucci, S.; Zampella, A. Novel Isoxazole Derivatives with Potent FXR Agonistic Activity Prevent Acetaminophen-Induced Liver Injury. *ACS Med Chem Lett* **2019**, *10* (4), 407-412. https://doi.org/10.1021/acsmedchemlett.8b00423.

(45) Maloney, P. R.; Parks, D. J.; Haffner, C. D.; Fivush, A. M.; Chandra, G.; Plunket, K. D.; Creech, K. L.; Moore, L. B.; Wilson, J. G.; Lewis, M. C.; Jones, S. A.; Willson, T. M. Identification of a Chemical Tool for the Orphan Nuclear Receptor FXR. *J Med Chem* **2000**, *43* (16), 2971-2974. https://doi.org/10.1021/jm0002127.

(46) Gege, C.; Kinzel, O.; Steeneck, C.; Schulz, A.; Kremoser, C. Knocking on FXR's Door:The

"Hammerhead"-Structure Series of FXRs Agonists - Amphiphilic Isoxazoles with Potent In Vitro and In Vivo Activities. *Curr. Top. Med. Chem.* **2014**, *14* (19), 2143-2158. https://doi.org/10.2174/1568026614666141112094430.

(47) Goodwin, B.; Jones, S. A.; Price, R. R.; Watson, M. A.; McKee, D. D.; Moore, L. B.; Galardi, C.; Wilson, J. G.; Lewis, M. C.; Roth, M. E.; Maloney, P. R.; Willson, T. M.; Kliewer, S. A. A Regulatory Cascade of the Nuclear Receptors FXR, SHP-1, and LRH-1 Represses Bile Acid Biosynthesis. *Mol Cell* **2000**, *6* (3), 517-526. https://doi.org/10.1016/s1097-2765(00)00051-4.

(48) Trauner, M.; Nevens, F.; Shiffman, M. L.; Drenth, J. P. H.; Bowlus, C. L.; Vargas, V.; Andreone, P.; Hirschfield, G. M.; Pencek, R.; Malecha, E. S.; MacConell, L.; Shapiro, D. Long-Term Efficacy and Safety of Obeticholic Acid for Patients with Primary Biliary Cholangitis: 3-Year Results of an International Open-Label Extension Study. *Lancet Gastroenterol Hepatol* **2019**, *4* (6), 445-453. https://doi.org/10.1016/s2468-1253(19)30094-9.

(49) Chiang, J. Y. L.; Ferrell, J. M. Up to Date on Cholesterol 7 Alpha-Hydroxylase (CYP7A1) in Bile Acid Synthesis. *Liver Res.* **2020**, *4* (2), 47-63. https://doi.org/10.1016/j.livres.2020.05.001.

(50) Renga, B.; Migliorati, M.; Mencarelli, A.; Cipriani, S.; D'Amore, C.; Distrutti, E.; Fiorucci, S. Farnesoid X Receptor Suppresses Constitutive Androstane Receptor Activity at the Multidrug Resistance Protein-4 Promoter. *Biochim Biophys Acta* **2011**, *1809* (3), 157-165. https://doi.org/10.1016/j.bbagrm.2011.01.008.

(51) Akwabi-Ameyaw, A.; Bass, J. Y.; Caldwell, R. D.; Caravella, J. A.; Chen, L.; Creech, K. L.; Deaton, D. N.; Jones, S. A.; Kaldor, I.; Liu, Y.; Madauss, K. P.; Marr, H. B.; McFadyen, R. B.; Miller, A. B.; III, F. N.; Parks, D. J.; Spearing, P. K.; Todd, D.; Williams, S. P.; Wisely, G. B. Conformationally Constrained Farnesoid X Receptor (FXR) Agonists: Naphthoic Acid-Based Analogs of GW 4064. *Bioorg. Med. Chem. Lett.* **2008**, *18* (15), 4339-4343. https://doi.org/10.1016/j.bmcl.2008.06.073.

(52) Mi, L.-Z.; Devarakonda, S.; Harp, J. M.; Han, Q.; Pellicciari, R.; Willson, T. M.; Khorasanizadeh, S.; Rastinejad, F. Structural Basis for Bile Acid Binding and Activation of the Nuclear Receptor FXR. *Mol. Cell* **2003**, *11* (4), 1093-1100. https://doi.org/10.1016/S1097-2765(03)00112-6.

(53) D'Amore, C.; Di Leva, F. S. S.; Sepe, V.; Renga, B.; Del Gaudio, C.; D'Auria, M. V. V; Zampella, A.; Fiorucci, S.; Limongelli, V. Design, Synthesis, and Biological Evaluation of Potent Dual Agonists of Nuclear and Membrane Bile Acid Receptors. *J Med Chem* **2014**, *57* (3), 937-954. https://doi.org/10.1021/jm401873d.

(54) Di Leva, F. S. S.; Festa, C.; D'Amore, C.; De Marino, S.; Renga, B.; D'Auria, M. V. V; Novellino, E.; Limongelli, V.; Zampella, A.; Fiorucci, S. Binding Mechanism of the Farnesoid X Receptor Marine Antagonist Suvanine Reveals a Strategy to Forestall Drug Modulation on Nuclear Receptors. Design, Synthesis, and Biological Evaluation of Novel Ligands. *J Med Chem* **2013**, *56* (11), 4701-4717. https://doi.org/10.1021/jm400419e.

(55) Wang, E.; Sun, H.; Wang, J.; Wang, Z.; Liu, H.; Zhang, J. Z. H.; Hou, T. End-Point Binding Free Energy Calculation with MM/PBSA and MM/GBSA: Strategies and Applications in Drug Design. *Chem. Rev.* **2019**, *119* (16), 9478-9508. https://doi.org/10.1021/acs.chemrev.9b00055.

(56) Yang, X.; Wang, J.; Chang, C.-Y.; Zhou, F.; Liu, J.; Xu, H.; Ibrahim, M.; Gomez, M.; Guo, G. L.; Liu, H.; Zong, W.-X.; Wondisford, F. E.; Su, X.; White, E.; Feng, Z.; Hu, W. Leukemia Inhibitory Factor Suppresses Hepatic de Novo Lipogenesis and Induces Cachexia in Mice. *Nat. Commun.* **2024**, *15* (1), 627. https://doi.org/10.1038/s41467-024-44924-w.

(57) Tacke, F. Targeting Hepatic Macrophages to Treat Liver Diseases. *J Hepatol* **2017**, *66* (6), 1300-1312. https://doi.org/10.1016/j.jhep.2017.02.026.

(58) Renga, B.; Mencarelli, A.; Migliorati, M.; Cipriani, S.; D'Amore, C.; Distrutti, E.; Fiorucci, S. SHP-Dependent and -Independent Induction of Peroxisome Proliferator-Activated Receptor-γ by the Bile Acid Sensor Farnesoid X Receptor Counter-Regulates the pro-Inflammatory

Phenotype of Liver Myofibroblasts. *Inflamm Res* **2011**, *60* (6), 577-587. https://doi.org/10.1007/s00011-010-0306-1.

(59) Skiniotis, G.; Lupardus, P. J.; Martick, M.; Walz, T.; Garcia, K. C. Structural Organization of a Full-Length Gp130/LIF-R Cytokine Receptor Transmembrane Complex. *Mol. Cell* **2008**, *31* (5), 737-748. https://doi.org/10.1016/j.molcel.2008.08.011.

(60) Schrödinger Release 2019-1: Maestro, New York, NY: Schrödinger, LLC, 2019.

(61) Shelley, J. C.; Cholleti, A.; Frye, L. L.; Greenwood, J. R.; Timlin, M. R.; Uchimaya, M. Epik: A Software Program for PK(a) Prediction and Protonation State Generation for Drug-like Molecules. *J Comput Aided Mol Des* **2007**, *21* (12), 681-691. https://doi.org/10.1007/s10822-007-9133-z.

(62) Banks, J. L.; Beard, H. S.; Cao, Y.; Cho, A. E.; Damm, W.; Farid, R.; Felts, A. K.; Halgren, T. A.; Mainz, D. T.; Maple, J. R.; Murphy, R.; Philipp, D. M.; Repasky, M. P.; Zhang, L. Y.; Berne, B. J.; Friesner, R. A.; Gallicchio, E.; Levy, R. M. Integrated Modeling Program, Applied Chemical Theory (IMPACT). *J Comput Chem* **2005**, *26* (16), 1752-1780. https://doi.org/10.1002/jcc.20292.

(63) Grippo, L.; Lucidi, S. A Globally Convergent Version of the Polak-Ribière Conjugate Gradient Method. *Math. Program.* **1997**, *78* (3), 375–391. https://doi.org/10.1007/BF02614362.

(64) Friesner, R. A.; Banks, J. L.; Murphy, R. B.; Halgren, T. A.; Klicic, J. J.; Mainz, D. T.; Repasky, M. P.; Knoll, E. H.; Shelley, M.; Perry, J. K.; Shaw, D. E.; Francis, P.; Shenkin, P. S. Glide: A New Approach for Rapid, Accurate Docking and Scoring. 1. Method and Assessment of Docking Accuracy. *J Med Chem* **2004**, *47* (7), 1739-1749. https://doi.org/10.1021/jm0306430.

(65) Cho, A. E.; Guallar, V.; Berne, B. J.; Friesner, R. Importance of Accurate Charges in Molecular Docking: Quantum Mechanical/Molecular Mechanical (QM/MM) Approach. *J. Comput. Chem.* **2005**, *26* (9), 915-931. https://doi.org/10.1002/jcc.20222.

(66) Sherman, W.; Day, T.; Jacobson, M. P.; Friesner, R. A.; Farid, R. Novel Procedure for Modeling Ligand/Receptor Induced Fit Effects. *J. Med. Chem.* **2006**, *49* (2), 534-553. https://doi.org/10.1021/jm050540c.

(67) Case, D.; Aktulga, H. M.; Belfon, K.; Ben-Shalom, I.; Berryman, J.; Brozell, S.; Cerutti, D.; Cheatham, T.; Cisneros, G. A.; Cruzeiro, V.; Darden, T.; Duke, R.; Giambasu, G.; Gilson, M.; Gohlke, H.; Götz, A.; Harris, R.; Izadi, S.; Izmailov, S.; Kollman, P. Amber 2022. 2022. https://doi.org/10.13140/RG.2.2.31337.77924.

(68) Maier, J. A.; Martinez, C.; Kasavajhala, K.; Wickstrom, L.; Hauser, K. E.; Simmerling, C. Ff14SB: Improving the Accuracy of Protein Side Chain and Backbone Parameters from Ff99SB. *J. Chem. Theory Comput.* **2015**, *11* (8), 3696–3713. https://doi.org/10.1021/acs.jctc.5b00255.

(69) He, X.; Man, V. H.; Yang, W.; Lee, T.-S.; Wang, J. A Fast and High-Quality Charge Model for the next Generation General AMBER Force Field. *J. Chem. Phys.* **2020**, *153* (11), 114502. https://doi.org/10.1063/5.0019056.

(70) Li, P.; Roberts, B. P.; Chakravorty, D. K.; Merz, K. M. J. Rational Design of Particle Mesh Ewald Compatible Lennard-Jones Parameters for +2 Metal Cations in Explicit Solvent. *J. Chem. Theory Comput.* **2013**, *9* (6), 2733-2748. https://doi.org/10.1021/ct400146w.

(71) Humphrey, W.; Dalke, A.; Schulten, K. VMD: Visual Molecular Dynamics. *J. Mol. Graph.* **1996**, *14* (1), 33-38. https://doi.org/https://doi.org/10.1016/0263-7855(96)00018-5.

(72) Pettersen, E. F.; Goddard, T. D.; Huang, C. C.; Couch, G. S.; Greenblatt, D. M.; Meng, E. C.; Ferrin, T. E. UCSF Chimera--a Visualization System for Exploratory Research and Analysis. *J Comput Chem* **2004**, *25* (13), 1605-1612. https://doi.org/10.1002/jcc.20084.

(73) Moraca, F.; Lupia, A.; Fiorillo, B.; Catalanotti, B. 3D Coordinates of the Isoxazole Derivative 3a against FXR and HLIFR Receptors. 2024. https://doi.org/10.5281/zenodo.13712504.

Table of Contents graphic